Sensitivity to Immune Checkpoint Blockade and Progression-Free Survival is associated with baseline CD8$^+$ T cell clone size and cytotoxicity

ONE SENTENCE SUMMARY

Using single-cell and bulk RNA sequencing we explore checkpoint immunotherapy activity on peripheral CD8$^+$ T cells in metastatic melanoma; demonstrating that cell subset and clone size determine gene expression responses to treatment, and that pre-treatment cytotoxicity and clonality of peripheral CD8$^+$ T cells is clinically prognostic.

Watson RA[1,2,3,⊗], Tong O[1,2,⊗], Cooper R[1,2], Taylor CA[1,2], Sharma PK[1,2], Verge de Los Aires A[1,2], Mahé EA[1,2], Ruffieux H[3], Nassiri I[1,2], Middleton MR[2,4], Fairfax BP[1,2,4,*]

1. MRC Weatherall Institute of Molecular Medicine, University of Oxford, Headington, Oxford, United Kingdom, OX3 9DU
2. Department of Oncology, University of Oxford, Old Road Campus Research Building, Oxford, United Kingdom, OX3 7DQ
3. MRC Biostatistics Unit, University of Cambridge, Cambridge Biomedical Campus, Cambridge, United Kingdom, CB2, 0SR
4. Oxford Cancer and Haematology Centre, Oxford University Hospitals NHS Foundation Trust, Churchill Hospital, Oxford, United Kingdom, OX3 7LE

[⊗] These authors contributed equally to this work

* To whom correspondence should be addressed:

Dr Benjamin Fairfax; benjamin.fairfax@oncology.ox.ac.uk

ABSTRACT

Immune checkpoint blockers (ICB) exert their anti-cancer effects via $CD8^+$ T cells, although how responses vary over sub-populations and across clones is incompletely understood. We performed single-cell RNA-sequencing of $CD8^+$ T cells and their receptors pre- and post-ICB across eight patients, integrating results with bulk-sequencing data (n=209). We identify seven subsets with divergent responses to ICB, finding the effector cluster demonstrates the most pronounced changes. Likewise, transcriptomic response to ICB relates to clone size, with large clones demonstrating increased numbers of regulated genes of higher immunological pertinence. Cytotoxic effector clones were more likely to persist long-term following ICB and overlapped with public tumour-infiltrating lymphocyte clonotypes. Notably, pre-treatment $CD8^+$ cytotoxicity associated with progression-free survival, highlighting the importance of the baseline $CD8^+$ immune landscape in long-term response. This work further advances understanding of the molecular determinants of ICB response and assists in the search for peripheral prognostic biomarkers.

INTRODUCTION

Antibodies binding the checkpoint proteins CTLA-4 (cytotoxic T-lymphocyte-associated protein-4) and PD-1 (programmed cell death protein-1) - Immune Checkpoint Blockers (ICB) - have revolutionised the treatment of metastatic melanoma (MM) and numerous other cancers*(1, 2)*. There is, however, marked heterogeneity in ICB-induced clinical benefit*(2)* and insights into determinants of ICB activity and variation in clinical response remain limited. Although tumour mutational burden has been linked to clinical outcome across multiple cancers*(3, 4)*, its absolute importance is unclear*(5)*. Similarly, the prognostically favourable association of tumour infiltrating lymphocytes (TILs) is long-established, but factors controlling T cell infiltration remain unresolved*(6, 7)*. Crucially, it is increasingly apparent that general aspects of the peripheral immune landscape may play a critical, yet comparatively under-investigated role in determining tumour recognition and control*(1, 2, 8)*.

$CD8^+$ T cells are cardinal to the immune response towards MM*(8, 9)*, with most research focussing on their presence within TILs*(10, 11)*. However, recent analysis of non-melanoma skin cancer indicates the T cell response to ICB derives from a distinct repertoire of T cell clones, denoted by shared carriage of specific T cell receptors (TCR), that migrate to the tumour upon treatment*(12)*. In MM patients, T cell clones can be observed to be shared across tumour and blood compartments *(11, 13–17)*, whilst the number of expanded clones (occupying >0.5% of the repertoire) in the periphery post first cycle of ICB treatment associates with long-term clinical outcome*(18)*. Thus, there is robust evidence that the peripheral clonal T cell response to ICB is informative as to anti-cancer immune responses and may allow for on-treatment prognostication. Much of these analyses have been performed agnostic to CD8 T cell phenotypes, and the determinants of ICB activity at the level of subsets and on a clone-by-clone basis are unresolved. The $CD8^+$ T cell ICB response has multiple components, including mitotic cell division*(19)* and increased cytotoxicity, as exemplified by interferon gamma (IFNγ) induction*(20)*, with the relationship between these being undefined. Interestingly, the magnitude of the mitotic response is not strongly linked to clinical outcome*(18)*. How these responses vary according to T cell phenotype*(21)*, their heterogeneity across clones, and if they are derived from novel or pre-existing

65 clones is unknown. To explore this we have used single cell RNA-sequencing (scRNA-seq) to track the
66 transcriptomic response of individual peripheral $CD8^+$ T cell clones to ICB, identifying baseline
67 markers of clonal sensitivity, and charting how response varies according to phenotypic subset and
68 clonal size. We demonstrate that $CD8^+$ T cell response to treatment with ICB varies according to
69 phenotypic subset and clonal size, with the cytotoxic effector subset showing increased responsivity but
70 remaining proportionally stable. Further dissection of ICB response at the clonal level reveals that clone
71 size markedly impacts magnitude of response, with large effector T cell clones developing enhanced
72 TCR signalling compared to other clones, and showing enrichment in melanoma TIL public clonotypes.
73 By tracking TCRs over longer periods of treatment we demonstrate expansion and survival of pre-
74 existing cytotoxic T cell clones, as well as markers of clonal persistence across cycles of treatment.
75 Finally, we apply these observations regarding baseline clone size and cytotoxicity to a large clinical
76 dataset, demonstrating that combining pre-treatment $CD8^+$ cell cytotoxicity and large clone count is
77 clinically prognostic, with individuals possessing both low cytotoxicity and fewer expanded clones
78 typically gaining significantly less benefit from treatment with ICB.

79

80 **RESULTS**

81 **Single-cell profiling of peripheral $CD8^+$ T cells from patients with metastatic melanoma**

82 We generated paired baseline (day 0 – 'C1') and on-treatment (day 21 – 'C2') 5' scRNA-seq and V(D)J
83 profiles across peripheral $CD8^+$ T cells from eight patients with MM undergoing treatment with cICB
84 (ipilimumab plus nivolumab, n=4) or sICB (pembrolizumab, n=4) (**fig. 1a; table S1; Methods**). In
85 total, 22,445 *CD3*/*CD8* expressing cells passed quality control, of which 17,909 cells had TCR
86 sequences. To identify distinct $CD8^+$ T cell populations, we performed unsupervised clustering,
87 observing globally similar UMAP projection of cells from both timepoints (**fig. S1a**), and subsequently
88 cross-referenced each cluster to identities from published $CD8^+$ T cell scRNA-seq datasets (**Methods**,
89 **fig. S1b-e**), grouping cells aligned to each identity together. Seven distinct groups of $CD8^+$ T cells were
90 identified (**fig. 1b-c**); Naïve, central memory (CM), effector memory (EM) and effector cells (ECs)

which collectively represent the majority of T cells, as well as highly cycling cells (Mitotic), γδ T cells (gd), and *KLRB1*-expressing mucosal-associated invariant T cells (MAIT), which formed a separate cluster from the rest of the cells. Mitotic cells had higher numbers of unique molecular identifiers (nUMI) and MKI67 expression per cell and a bias towards S and G2M cell cycle phases (**fig. S1f-g**), consistent with previous descriptions *(13, 22)*. Expression of *TRDC* was used to identify the γδ subset *(23)*, which was enriched for *KLRC3*, *KIR3DL2* and *KIR3DL3* (**fig. 1c**). To distinguish the biological features of each subset, we performed Gene Ontology Biological Process (GOBP) enrichment analysis (**fig. 1d**), which highlighted key immune pathways including *IFNG* signalling and T cell activation/co-stimulation were enriched in EM and ECs, consistent with higher cytotoxicity (**fig. S1h**). In contrast, Naïve/CM and Mitotic subsets demonstrated upregulated translational and mitochondrial machinery. We further examined the expression of T cell exhaustion markers across the cell subsets (**fig. 1e**). Increased expression of *TOX* and *HAVCR2* and most other exhaustion-related genes resulted in distinct grouping of Mitotic, ECs, EM and γδ cells from the remaining subsets. *PDCD1* expression being highest in EM and Mitotic cells, indicating greater intrinsic exhaustion within these subsets. The majority of *PDCD1*$^{+}$ cells co-expressed *TIGIT* (**fig. 1f**), and EM and Mitotic cells, but not ECs, were enriched within this PDCD1^{+} TIGIT^{+} population (Fisher's exact test, **fig. 1g**).

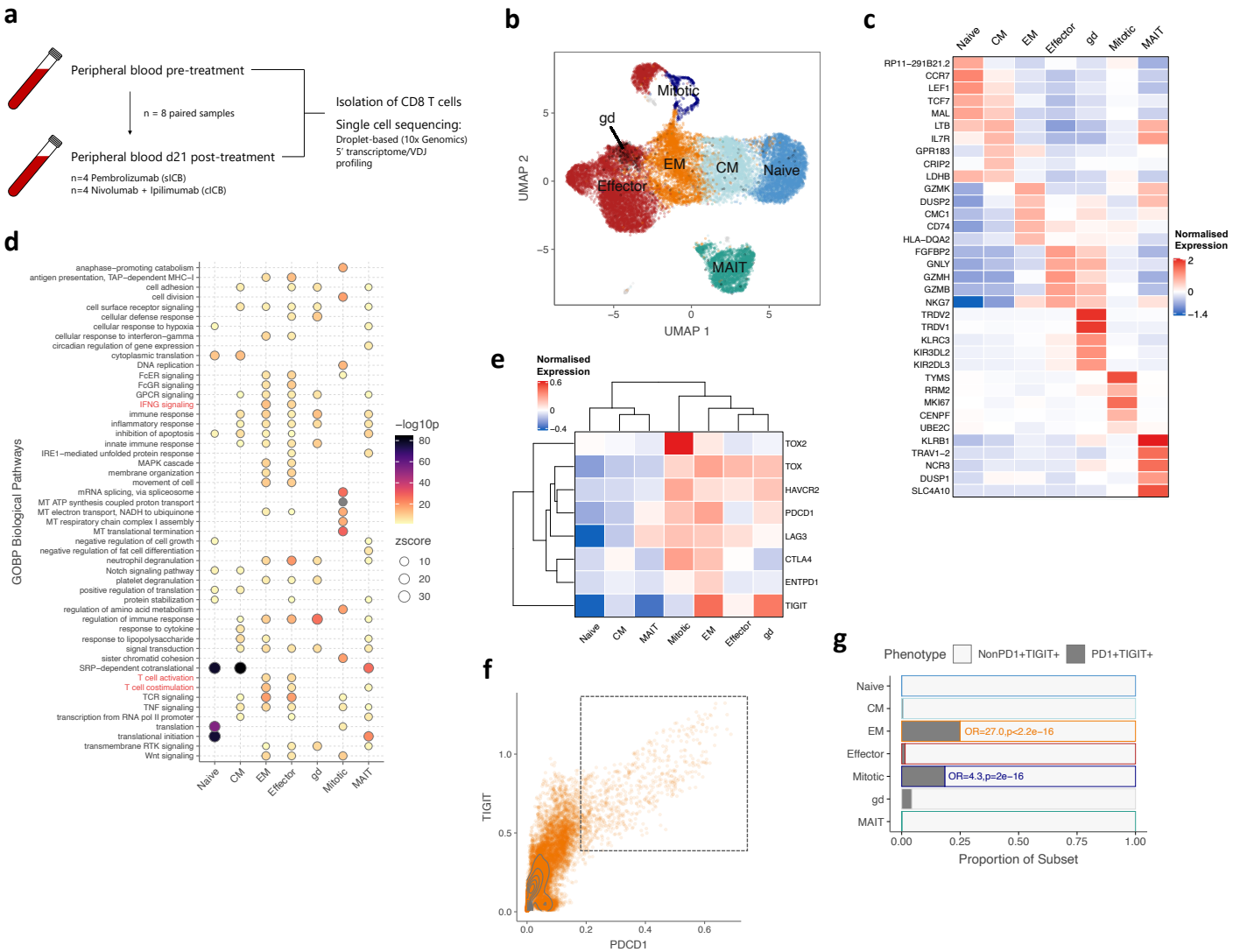

Figure 1: **Identification of peripheral CD8$^+$ T cell subsets in metastatic melanoma before and during ICB. (a)** Workflow for sample collection and processing for scRNA-seq. **(b)** UMAP clustering of n=22,445 peripheral CD8$^+$ T cells from n=8 individuals sampled at pre-treatment and following 21 days of ICB, across seven distinct subsets as represented by each colour. **(c)** Expression heatmap showing distinct gene expression profiles for the identified subsets. Genes were selected as the five most differentially-expressed genes by p-value present at both pre-treatment and at 21d post-ICB for each timepoint. **(d)** Dot plot heatmap showing Gene Ontology Biological Process (GOBP) terms significantly enriched across each subset (adjusted p-value < 0.05); selected pathways highlighted in red. **(e)** Expression heatmap of selected T cell activation and exhaustion markers. **(f)** Dot plot of imputed *PDCD1* and *TIGIT* expression across CD8$^+$ T cells, with the indicated PD1$^+$ TIGIT$^+$ peripheral exhausted (Ex) population. **(g)** Subset proportions of non-exhausted and exhausted cells, showing an enrichment of EM and mitotic cells by Fisher's exact test (odds ratio > 1).

120 **Changes in CD8$^+$ T cell subset composition during early immune checkpoint blockade**

121 Focussing on the key subsets (Naïve, CM, EM, EC and Mitotic), we first assessed ICB effects on CD8$^+$
122 T cell compartment composition. We found ICB significantly reduced CM proportion (**fig. 2a**), whilst
123 other subsets remained relatively unchanged. To explore the generalisability of these findings across a
124 larger cohort we developed composite expression signatures for each single-cell subset (**Methods**),
125 characterising them in bulk RNA-sequencing data generated from similarly derived MM patient CD8$^+$
126 T cells*(18)* (n=212 paired C1/C2 samples from 106 individuals). For most single-cell samples (15/16),
127 bulk RNAseq was generated, permitting validation of score-inferred proportions, with significant
128 correlation between bulk expression scores and the single-cell proportions across all subsets (**fig. S2a**).
129 Across the cohort, naïve, CM and mitotic scores anti-correlated with age, whilst EM and EC scores
130 were correlated, in keeping with known ageing effects *(24)* (**fig. S2b**). Notably, whilst ICB reduced
131 naïve and CM expression scores and increased EM and mitotic scores (**fig. 2b**), no significant change
132 in the EC score was observed, indicating the EC subset remains stable. The increase in mitotic score
133 post-ICB remained sustained at C4 (d63) of treatment (**fig. S2c**). Finally, the decrease in naïve and CM
134 score was strongly correlated within individuals, and inversely correlated with mitotic score increase
135 (**fig. S2d**). Changes in EC score correlated with EM, and to a lesser extent, mitotic score, indicating
136 shuttling from these subsets into the mitotic pool, potentially allowing for EC compartment
137 replenishment post-ICB.

138

139 We then examined how TCR clones composed of more than one cell are distributed across subsets at
140 C1 and C2 (**fig. 2c**). Most of these clones were of an EC phenotype, being detected in this subset at both
141 timepoints, and whilst there was emergence of novel EM and EC clones at C2, notably few clones were
142 shared across subsets at either timepoint *(14, 22)*. To further characterise the Mitotic cells, we tracked
143 their clonal dynamics between C1 and C2. Interestingly, most Mitotic cells represent small clones, with
144 the median clone size being similar to Naïve and CM cells (**fig. S2e**) and not changing with treatment.
145 Expanded clones were not enriched in the Mitotic subset, and were relatively depleted in Naïve and CM

146 subsets post-treatment (**fig. 2d**, **table S4**). In general, whilst there was limited TCR sharing between
147 memory cells and ECs across timepoints, most resampled clones remained in the same subset over time
148 (**fig. 2e**), the exception being the Mitotic subset where only 2.2% of C2 Mitotic clones were present in
149 any subset at C1. Altogether, the observed changes in subset proportion can be summarised by **(i)** a
150 relative increase in EM cells through both emergence and expansion of pre-existing clones (**fig. 2b, 2c,**
151 **1h**), a small proportion differentiating from C1 ECs; **(ii)** stability in the EC compartment size
152 accompanied by changes in clonal dispersion, with expansion of a subset of EC clones (**fig. 2b, 2c**)
153 counterbalanced by reduced median EC clone size (**fig. S2f**); **(iii)** an increase of cells in a mitotic state,
154 the majority of which are small clones not sampled at both timepoints (**fig. 1h, 2b, 2d**), indicating that
155 most Mitotic cells do not establish significant clonal populations; and **(iv)** a relative loss of Naïve and
156 CM cells (**fig. 2b**) following ICB.

157 **Figure 2. Dynamic immune composition changes upon ICB. (a-b)** Changes in the proportion of
158 each cell subset between pre-treatment (C1) and 21d post-ICB (C2) as determined by scRNA-seq
159 (n=8, two-sided Wilcoxon-signed rank test) **(a)** or inferred from bulk RNAseq data (n=110, two-sided
160 Wilcoxon-signed rank test) **(b)**. For the bulk RNAseq inference, subset scores were calculated for

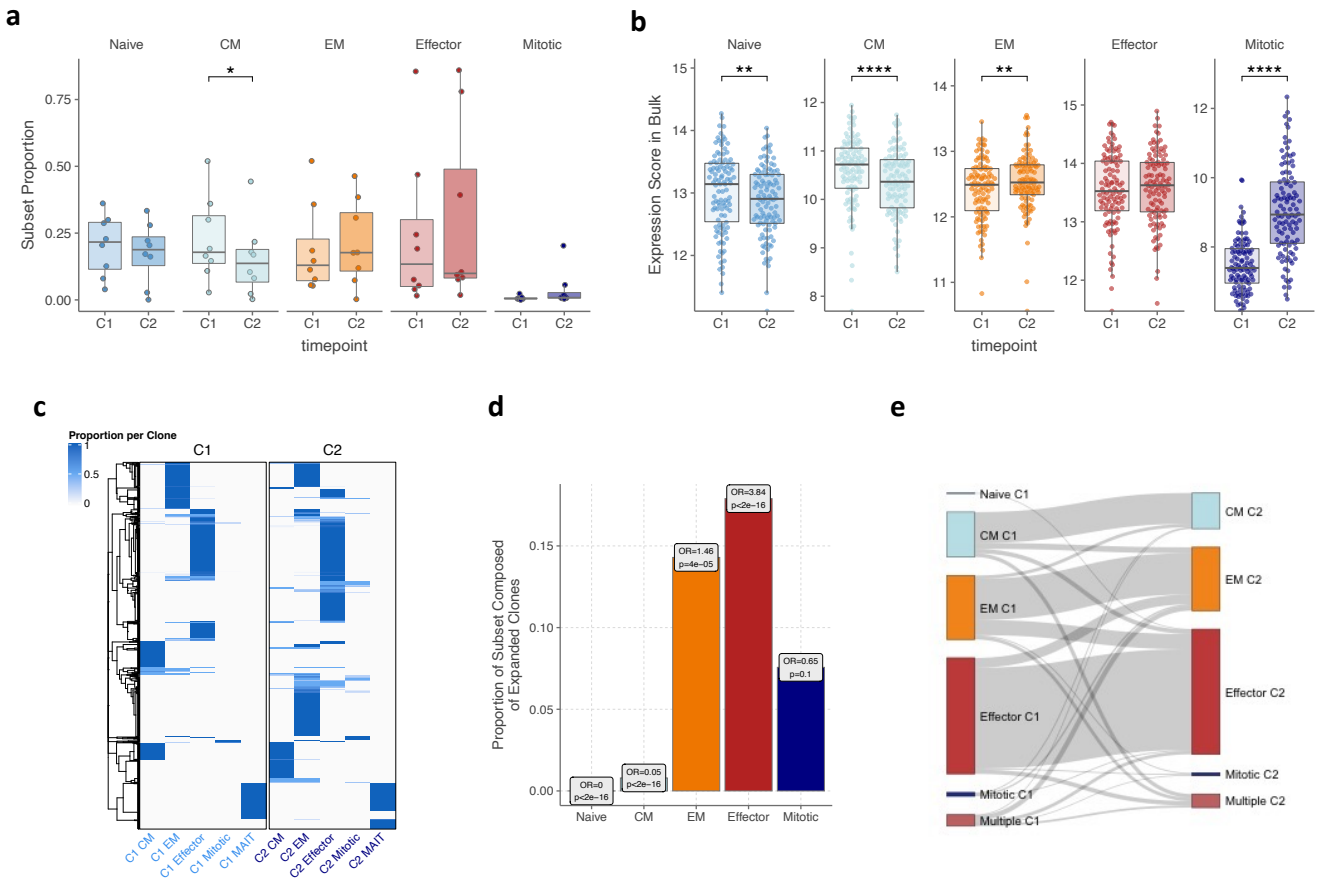

each bulk RNAseq sample based on a list of markers that distinguished each subset at both pre-treatment and 21d post-ICB in the scRNA-seq data (Methods, Supplementary Fig. 2a-b). **(c)** TCR sharing heatmap between C1 and C2 CD8+ T cell subsets, showing T cell clones consisting of more than 1 detected clone and their relative presence and subset proportions at each timepoint. **(e)** Proportion within each subset at C2 of clones that have significantly expanded from C1 (Fisher's exact test). **(f)** Sankey plot tracking the cell subset phenotype of C1 clones at C2. For each clone, the subset in which most of its members were present in at a given timepoint was designated as the predominant subset for that clone; 'multiple' indicates clones equally distributed across multiple subsets. The width of the connecting flowline represents the number of clones with the respective C1 and C2 subset phenotypes.

Effector CD8$^+$ T cells show increased sensitivity to immune checkpoint blockade

We further characterised responses to ICB between C1 and C2 at a sub-population level, focusing on Naïve, CM, EM and ECs. We controlled for increased power to detect differentially expressed (DE) genes (comparing pre- to post-treatment) in larger subsets by subsampling varying numbers of cells across each subset (analysis bootstrapped 100 times), and used multiple DE analysis pipelines (Methods). Across the four subsets, ECs had more DE genes with treatment irrespective of subsample size (**fig. 3a**). When we used a linear model with an interaction term to control for inter-individual variation we made similar observations (**fig. S3a**). To quantify these patterns of DE, we used a cut-off of n=1100 cells per subsample (**Methods**), and calculated the frequency of genes being detected as significant (adjusted p-value below 0.05) across one hundred bootstraps. Genes such as *IL10RA* and *GZMA* were consistently down- and up-regulated by treatment in all bootstraps in ECs, but not in other subsets (**fig. S3b, table S6**). Comparing the DE genes in ECs versus other subsets, we observed that many were exclusively modulated in this subset (**fig. S3c**), suggesting ICB has a distinct effect on these cells. Subset-wise GOBP analysis of the induced and suppressed genes demonstrated that the most modulated pathways were either conserved pathways represented across all subsets, or specific to ECs (**fig. 3b**). Specifically, pathways restricted to ECs encompassed pro-inflammatory and immune pathways including NFκB, MAPK and TNF signalling (**fig. S3d**), further supporting the profound immune-stimulatory effect of ICB on this subset.

191 **CD8$^+$ T cell clones differentially modulate gene expression post-ICB as a function of their size**

192 Given our previous findings linking the number of large clones with clinical outcome, we sought to
193 understand the relationship between the size of a clone and its response to ICB. We grouped clones into
194 four categories according to their size as a proportion of the total repertoire (**fig. 3c**). As expected, most
195 Naïve cells were of the smallest sizes, whereas the larger clone categories were composed of ECs and,
196 to a lesser extent, EMs (**fig. 3c**). We next assessed the relationship between clonal size and ICB effect
197 by performing category-wise DE analysis across treatment (including only clones present at both
198 timepoints, agnostic to subset type), using sampling to control for variation in cell number across sub-
199 population and timepoint, bootstrapping analysis 100 times. This produced a response pattern of DE
200 genes according to clone size, with small and medium-sized clones having comparatively fewer DE
201 genes than large and very large clones (**fig. 3d**).

202 Given this analysis is potentially confounded by differing subset proportions in each size category, we
203 repeated this process restricted to EC and EM subsets, with clonal size simply dichotomized with a cut-
204 off of 0.5% of the repertoire to denote large from small. The previously observed pattern was preserved
205 within each subset, with larger clones again showing greater numbers of DE genes following ICB
206 compared to smaller clones (Wilcoxon test, $p<0.0001$, **fig. 3e**). These findings were replicated upon
207 sequential exclusion of each individual in the cohort, suggesting that they are not simply a feature of
208 inter-individual variation (**fig. S3e**).

209 To understand these effects at a functional level, we analysed GOBP pathways corresponding to the DE
210 gene sets within the EC and EM subsets (**fig. 3f, g; table S7**). We again noted that large EC clones had
211 a strikingly divergent gene expression profile following ICB compared to both small EC clones (**fig.**
212 **3f**) and large EM clones (**fig. 3g**), with pathways including T cell activation, proliferation and co-
213 stimulation, TCR signalling, and IFNγ production uniquely upregulated in large ECs.

214 Taken together, we find clonal size influences both the magnitude of response to ICB as well as the
215 types of genes regulated, and this phenomenon is observed even within the same phenotypic subset.

216 Larger clones display marked enhancement of immune function following ICB treatment, with large
217 ECs uniquely upregulating a number of immune pathways critical to the ICB response.
218

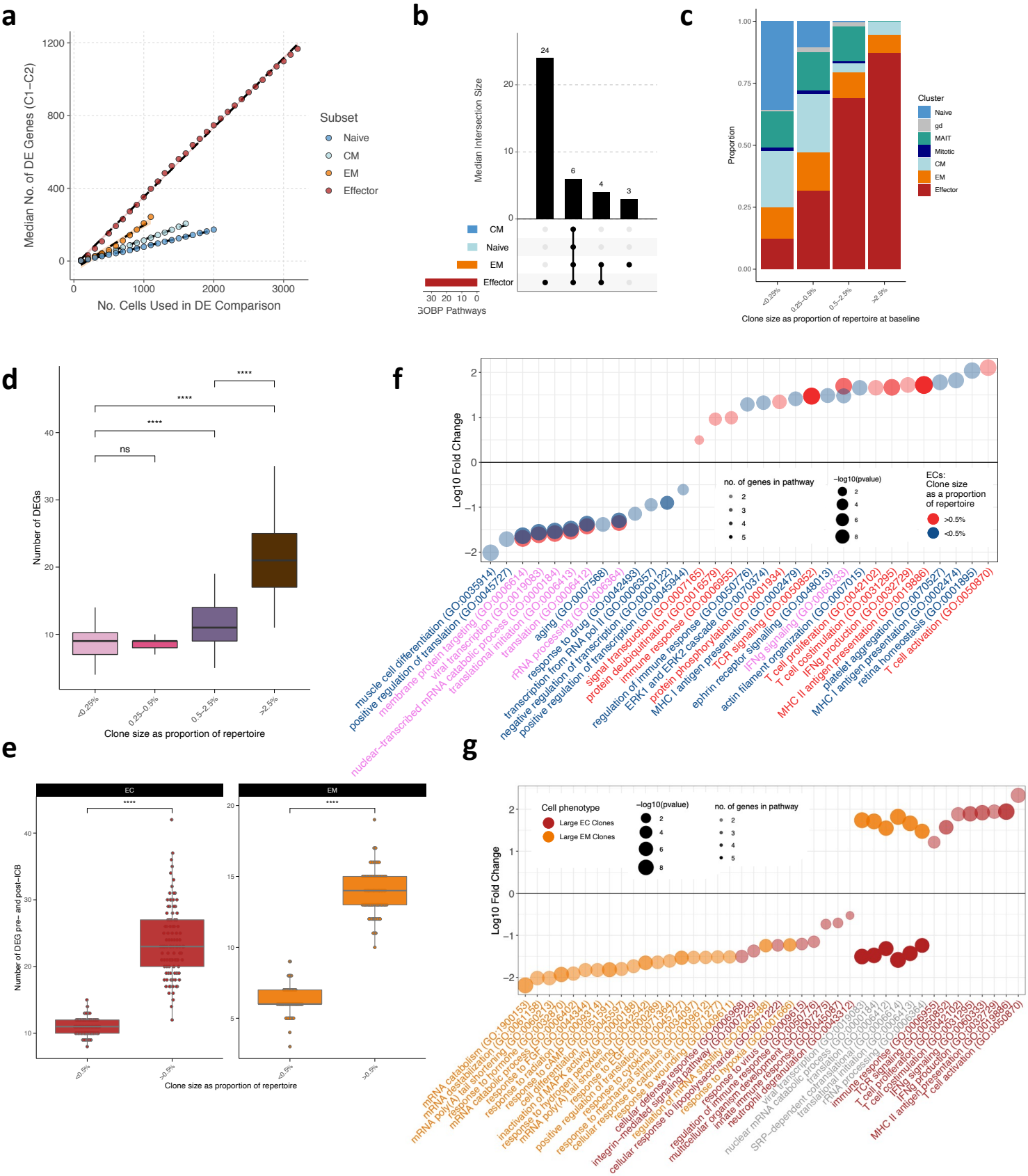

Figure 3. Subset-specific and clone-size dependent transcriptome changes upon ICB. (a) Median number of differentially expressed (DE) genes across 21 days of ICB in conventional T cell subsets. Each subset was subsampled to the indicated number of cells at C1 and C2 and tested for DE genes

223 across 100 bootstraps. At each n-value for number of cells, there was a significant difference across the
224 subsets in the number of DE genes ($p<0.0001$, unpaired Wilcoxon test). **(b)** Upset overlap plot of GOBP
225 pathways upregulated in each subset following treatment (subsample of n=1100 cells), based on the DE
226 genes per bootstrap in (a). The median number of pathways in each intersecting set was calculated over
227 the 100 bootstraps. **(c)** Clonal size bins at C1 filled by proportion of each phenotypic cluster. **(d)** Number
228 of DE genes pre- and post- treatment per clonal size bin. Each clonal size bin was subsampled to a
229 constant size and the analysis bootstrapped 100x. **(e)** Number of differentially expressed genes pre- and
230 post- treatment for large vs small ECs (red) and EMs (orange). Each cluster was subsampled to a
231 constant size and the analysis bootstrapped 100x. **(f)** GOBP analysis demonstrating pathways up- and
232 down-regulated in large vs small ECs pre- and post- treatment. Large ECs are coloured in bright red,
233 small ECs in blue. Pathways where the text is in purple represent those that are shared between both
234 groups. **(g)** GOBP analysis demonstrating pathways up- and down-regulated in large ECs (red) vs large
235 EMs (orange) pre- and post- treatment. Pathways where the text is in grey represent those that are shared
236 between both groups. For all analysis comparing numbers of DE genes, p-values were determined by
237 two-sided Wilcoxon rank-sum test.
238

239 **Cytotoxic clones demonstrate propensity to persist post-ICB treatment**

240 To further understand the temporal dynamics of clones we tracked the presence or absence of each
241 clone across C1 and C2, restricting the analysis to clones composed of two cells or more. Perhaps
242 unsurprisingly, large clones were more likely to be resampled, with clones only sampled at one
243 timepoint predominantly grouped within smaller size categories (**fig. 4a**). Genes correlated with IFNγ
244 are informative as to cytotoxicity. We therefore adopted previous methods (13) to develop a cytotoxicity
245 score for each cell based on key IFNγ correlated genes. We find that whilst cytotoxicity was globally
246 increased at C2, clones sampled at both timepoints or only at C2 show increased cytotoxicity over those
247 present only at C1 (**fig. 4b**). This finding was robust to separating clones on their size (**fig. S4a**). To
248 explore these observations further we examined baseline (C1) profile of clones, grouping those
249 significantly shrinking (as per a Fisher's exact test, see **Methods**) or absent at C2 as 'involuting' clones.
250 We contrasted these with clones that were found to expand or showing no significant change in size
251 (stable). Interestingly, small clones that subsequently expanded or remained stable following ICB were
252 significantly more cytotoxic at baseline than those that involuted (**fig. 4c**). This finding was similarly
253 observed if we determined change to clone size by simple fold change (**Methods**, **fig. S4b**). This
254 difference in baseline cytotoxicity across involuting and non-involuting clones was not seen within
255 larger clones, which were overall significantly more cytotoxic than smaller clones (**fig. 4c**). As such,
256 these findings suggest that following ICB there is an overall increase in cytotoxicity which is driven by

257 a combination of the persistence of pre-treatment cytotoxic T cell clones, involution of clones with low
258 cytotoxicity and the emergence of more cytotoxic clones.

259 To extend analysis across later timepoints, we examined bulk RNA-seq data from $CD8^+$ T cells isolated
260 63-106 days post-treatment (C4+), available for six out of the eight individuals for which scRNA-seq
261 data was available (**Methods**). From the corresponding TCRs identified in these samples, we found 992
262 overlapping unique-TCRβs associated with 4,245 cells at C2 within the scRNA-seq data. Notably, clone
263 size at C2 and C4+ were highly correlated (Spearman's rho=0.84, $p<2.2x10^{-16}$, **fig. 4d**), indicating
264 relative preservation of clonal structure over this longer period. Comparison of C2 clones (minimally 2
265 cells in size) that expanded or remained stable versus those that involuted between C2 and C4+
266 highlighted an enrichment for ECs in the stable/expanding group (OR 1.6, p=0.023) whilst there was
267 under-representation of EMs (OR 0.61, p=0.0047) (**fig. 4e**). We subsequently constrained further
268 analysis to the EC subset, analysing C2 cytotoxicity of stable/expanding clones versus those involuting
269 by C4+. Again we found a significantly higher cytotoxicity in those stable or expanding (**fig. 4f**), and
270 this was robust to alternatively defining changes to clone size based on fold change, rather than by a
271 Fisher's test (**fig. S4c**). Notably, this trend persisted when clones were grouped based on their size (**fig.
272 S4d**), although was not statistically significant for the large clones, likely reflecting underpowering.
273 Finally, by comparing expression of EC clones stable/expanding between C2 to C4+ to those that
274 involuted we identify genes linked to clonal stability. Intriguingly, we find killer lectin receptor genes
275 including *KLRF1* (Killer Cell Lectin Like Receptor F1), *KLRC2/3*, and the marker *TIGIT*, were amongst
276 those significantly higher in stable/expanding ECs at C2, whilst downregulated genes included *STAT1*
277 **(fig. 4g, table S8**), suggesting these may form markers of clonal persistence.

278 Collectively, these results indicate that pre-existing cytotoxicity belies increased clonal persistence,
279 with increased C1-C2 persistence of clones that are more cytotoxic at baseline, whilst emerging clones,
280 although small, also possess higher levels of cytotoxicity. Similarly, within the EC compartment, C2
281 cytotoxic clones have increased likelihood to be found at d63+ of treatment.

282

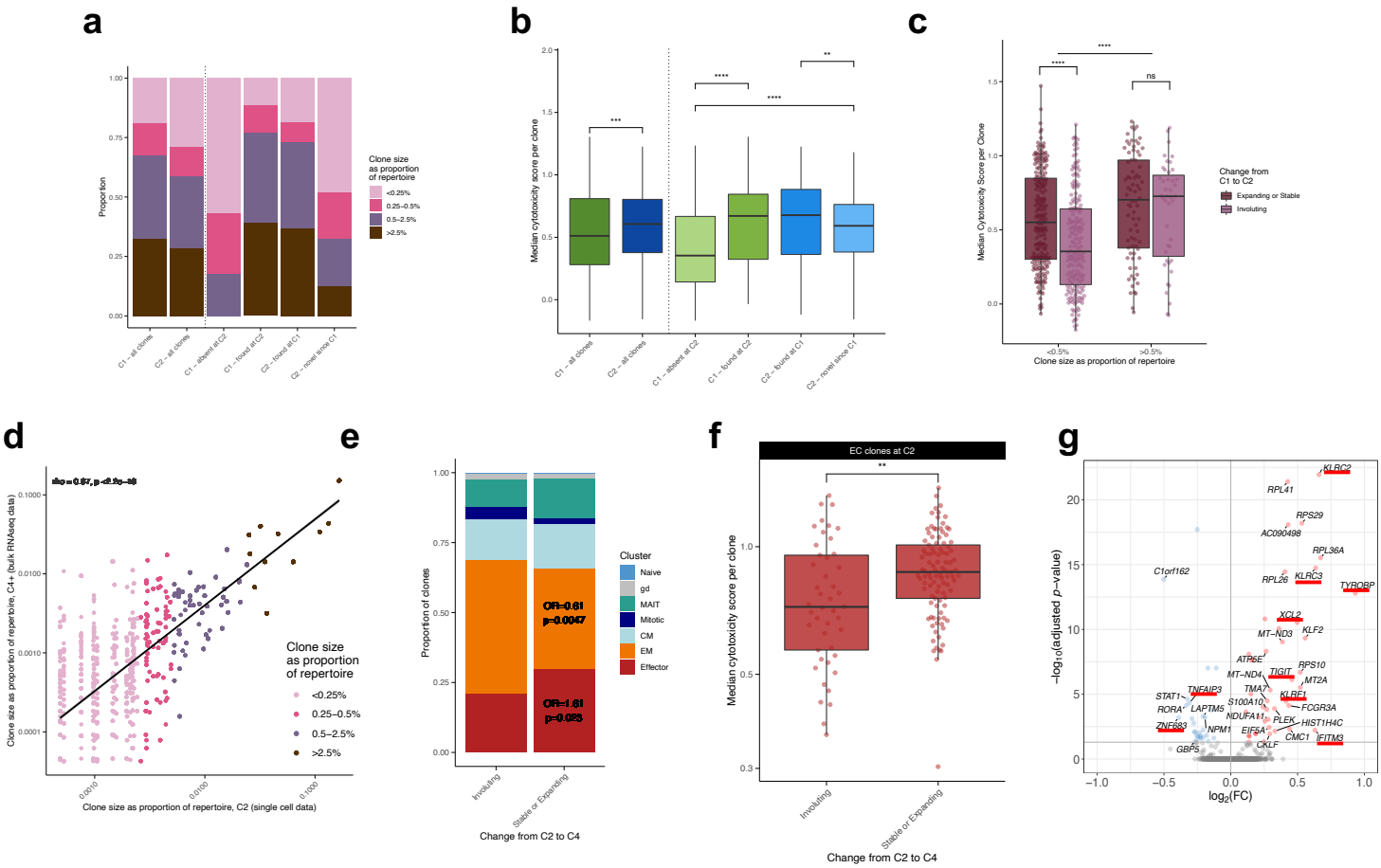

Figure 4. Cytotoxic clones demonstrate propensity to persist post-ICB treatment. (a-b) Proportion of clonal size groupings (a) and median cytotoxicity per clone (b) for clones found at both C1 and C2 versus at just at one timepoint, compared to all clones at C1 and C2. **(c)** Median cytotoxicity per clone for those present at C1 that subsequently expand/remain stable (dark purple) or involute (light purple) by C2. Clones are separated based on size using a cut-off of 0.5% of the repertoire to denote large from small. The horizontal line demonstrates the significant difference between all large compared to all small clones. **(d)** Clone size at C2 compared to size at C4+; each point denotes a clone and is coloured based on size grouping at C2 (Spearman's correlation). **(e)** Proportion of clones that are stable/expanding or involuting from C2 to C4+ coloured by their phenotypic cluster; odds ratios for the proportion of ECs and EMs in the expanding/stable compared to the involuting group (Fisher's exact test). **(f)** Median cytotoxicity score per clone across EC clones found at C2 that subsequently expand/remain stable or involute by C4+. **(g)** Volcano plot of genes differentially expressed by ECs at C2 that subsequently expand/remain stable by C4+ compared to those that involute; genes of interest are denoted with an underscore. The direction is in favour of clones that expand/remain stable – i.e., those in red with a positive FC are upregulated in clones that expand/remain stable. For all analyses, only clones with >1 cells were included, with unpaired Wilcoxon tests used for all comparisons unless otherwise stated.

Baseline and early on-treatment cytotoxicity is prognostic for clinical outcome during ICB

Given that baseline cytotoxicity delineates cells likely to persist or expand during ICB, potentially reflecting response to antigen, we explored the relationship between both pre and on-treatment $CD8^+$ T cell cytotoxicity and clinical response to ICB. We generated cytotoxicity scores for each bulk

306 sequencing sample in our cohort (n=131 at C1 and n=109 at C2, **Methods**) which we separately
307 validated with flow cytometry across a subset of samples, finding strong correlation of the cytotoxicity
308 score with expression of cytotoxic markers such as perforin-1 (**fig. S5a-b**). Whilst cytotoxicity at C1
309 was strongly-correlated with C2 cytotoxicity across the cohort, indicative of the importance of the
310 baseline response (**fig. S5c**), ICB tended to increase cytotoxicity, with a larger effect from cICB **(fig.**
311 **S5d**).

312 Patients had significantly higher $CD8^+$ cytotoxicity pre-treatment compared to healthy controls (**fig.**
313 **5a**), reflecting the systemic immune effects of MM. Of note, in patients who proceeded to respond to
314 treatment, both C1 and C2 cytotoxicity was higher than in those progressing by six months. Using
315 Kaplan-Meier estimates (log-rank test), we found a cytotoxicity score above the cohort median at either
316 baseline or C2 construed increased progression free survival (PFS) (**fig. 5b**, **S5e**), supporting the finding
317 that baseline immune profile is important in determining clinical outcome, and demonstrating that
318 agnostic sampling of the peripheral $CD8^+$ subset provides prognostic information. In contrast, we found
319 no association between the mitotic score and PFS at either C1 or C2 (p=0.78 and 0.69 respectively, log-
320 rank test, data not shown), suggesting the degree of baseline CD8+ T cell division, or that induced by
321 ICB, does not relate to clinical benefit.

322 Having previously shown that the number of large clones at C2 is associated with clinical response to
323 ICB*(18)*, we explored whether $CD8^+$ cytotoxicity could be integrated with large clone count to stratify
324 patients according to outcome *prior* to treatment. First, we recapitulated in this expanded cohort the
325 finding that C2 but not C1 large clone count is strongly associated with PFS, with increased significance
326 in the cohort as it expands and matures (**fig. S5f**). As expected, $CD8^+$ cytotoxicity score correlated with
327 large clone count across healthy individuals, C1 and C2 samples (**fig. 5c**), whilst responding individuals
328 had significantly higher cytotoxicity irrespective of large clone count when assessed with a linear model
329 (**fig. S5g**). We next explored whether cytotoxicity and large clone count could additively predict six-
330 month patient outcome using a linear discriminant analysis (LDA) model. This yielded an area under
331 the receiver operating characteristic curve (AUC) of 0.69 (**fig. S5h**), but did not seem to be co-
332 operatively affected by cytotoxicity or large clone count (**fig. S5i**). Instead, given the close association

333 between the two measures, we wondered whether they had a compensatory interaction. We grouped
334 individuals on a combination of above/below median large clone count and cytotoxicity and examined
335 their PFS on this basis. We found that individuals with below both median large clone count *and* median
336 cytotoxicity (Group 4) at baseline had significantly lower PFS compared to all other groups (**fig. 5d**)
337 which otherwise had comparable survival; this effect also being observed at d21 (**fig. S5j**). As such, we
338 further stratified a subset of patients with low pre-treatment peripheral $CD8^+$ T cell activity, with limited
339 clonal expansion and low cytotoxicity, that receives minimal clinical benefit from treatment with ICB.

340

341 **Validation using external datasets**

342 In order to establish the validity of our findings and apply them more generally, we sought relevant
343 published datasets. To explore the prognostic value of cytotoxicity score in an alternative context we
344 looked to see whether our observations extended to the tumour environment. Utilising the Riaz dataset
345 of paired RNA-seq and TCRB-seq data from melanomas prior to and during treatment with anti-PD-
346 1*(25)*, we devised an intratumoral $CD8^+$ T cell cytotoxicity score by selecting genes used in our
347 peripheral cytotoxicity analyses that showed strongest correlation with *CD3D*, *CD3E*, *CD8A*, *CD8B*,
348 *IFNG* and *PRF1* expression (**fig. S6a**), and subsequently identified the number of TCRB clones per
349 sample with proportion above 0.5%. Despite the low number of individuals in this cohort, we found
350 significantly lower overall survival for patients with below median large clone count and cytotoxicity
351 (**fig. 5e**) at baseline.

352 Given this concordance between the peripheral and intratumoral T cell state, we used an alternative
353 dataset of TCRB chains sequenced from melanoma biopsies *(26)*. From the 199 samples, 85,528 unique
354 TCRB were identified, of which 392 were found in our samples. We assessed the characteristics of cells
355 carrying one of these known tumour-infiltrating beta chains at both timepoints and found these
356 contained a significantly increased proportion of ECs compared to other cells subsets (**fig. 5f, S6b**).
357 Within these 'TIL-TCR' ECs, there was additionally a significantly higher proportion of large clones
358 (**fig. 5g, S6d**) with higher cytotoxicity score at both timepoints (**fig. 5h, S6c**). Extending these
359 observations to our bulk cohort, we also observed greater clonal expansion of TIL-TCR matching T cell

clones in patients compared to healthy controls (**fig. S6e**). Notably, when we compared this to the profile of cells matching public viral-reactive TCRs *(27)* (n=149 cells), clonally expanded ECs were under-represented, and there was no significant difference in cytotoxicity (**fig. S6f-h**). Together, this supports our findings of the importance of large, peripheral EC clones which appear to be over-represented within the tumour-infiltrating compartment.

Figure 5. CD8$^+$ T cell cytotoxicity is associated with clinical response to ICB. (a) Cytotoxicity calculated in CD8$^+$ bulk RNA-seq samples is significantly higher in responding patients than progressor

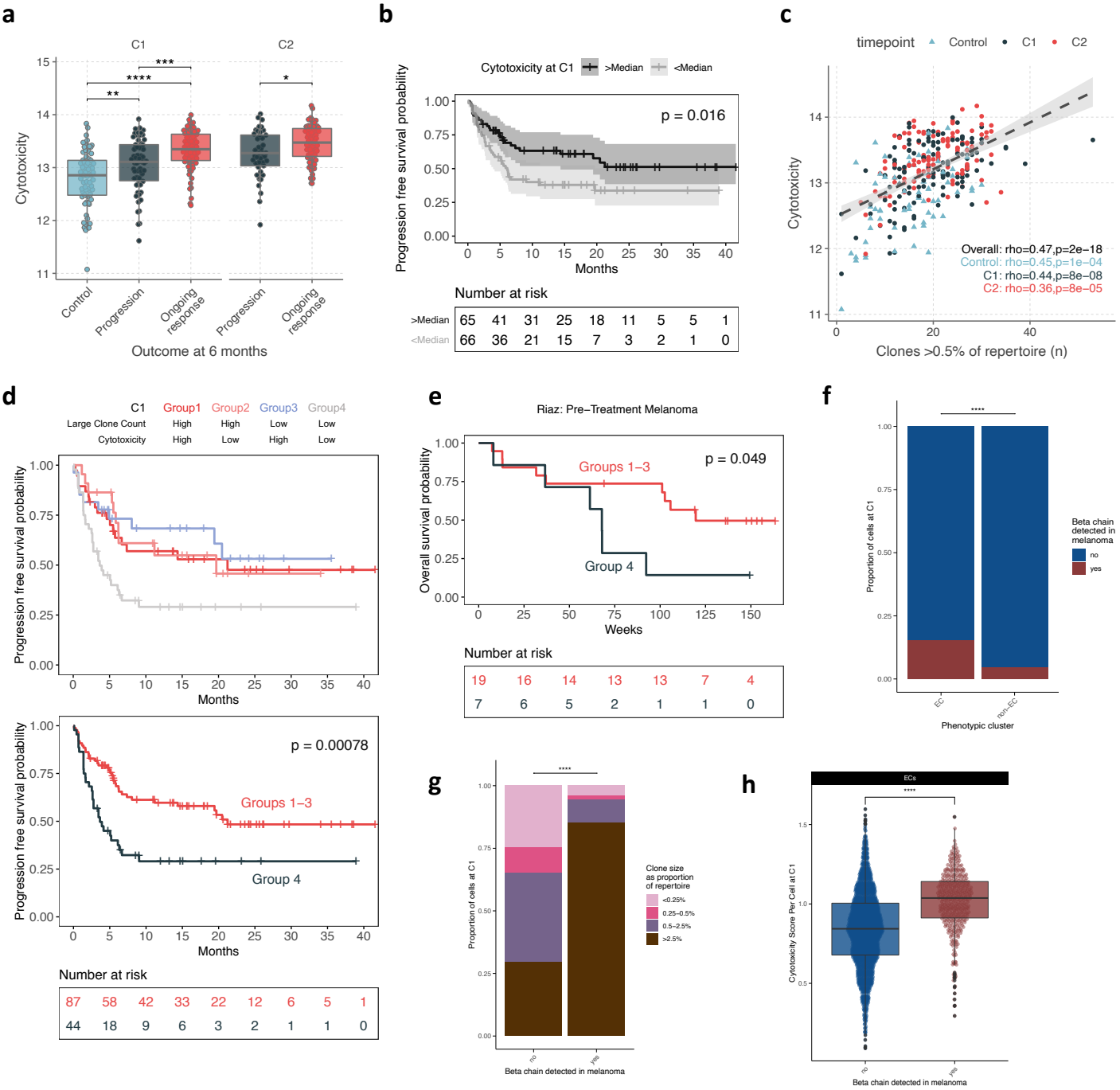

and control individuals at pre-treatment and d21 (n=69 controls, 112 patients). **(b)** Kaplan-Meier curves showing increased progression free survival in patients with baseline cytotoxicity above median (n=131 patients) (two-sided log-rank test). **(c)** Correlation between large clone count and cytotoxicity score in the bulk cohort, across control individuals and patients at C1 and C2 (n=69 controls, 137 patients, Spearman's rank test). **(d)** Progression free survival in patients separated by a combination of C1 large clone count and cytotoxicity (above/below median) (n=131, two-sided log-rank test; Group1 vs Group4, p=0.019; Group2 vs Group4, p=0.023; Group3 vs Group4, p=0.010). **(e)** Analysis of overall survival in melanoma patients from Riaz et al. 2017*(25)* based on intratumoral RNAseq and TCRB-seq data. Patients were separated by a combination of pre-treatment large clone count (TCRB-seq) and cytotoxicity (RNAseq) (above/below median, as in (d)) (n=26, two-sided log-rank test). **(f)** Proportion of ECs compared to non-ECs at C1 that carry a tumour-infiltrating TCRB chain, as identified by TCRseq of resected melanomas by Pruessman et al. 2020*(26)* (Fisher's exact test). **(g)** ECs at C1 that are either tumour-infiltrating or not, filled by their clonal size; Fisher's exact test for the proportion of large clones (>0.5%) compared to small clones found in the tumour-infiltrating and not-tumour-infiltrating compartments. **(h)** Cytotoxicity scores of ECs at C1 categorised by whether they carry a tumour-infiltrating TCRB chain or not (unpaired Wilcoxon test).

DISCUSSION

Identifying the cells most responsive to ICB is vital in understanding the mechanisms of ICB response and resistance. In this study we have addressed the peripheral $CD8^+$ T cell response to ICB at a single-cell level, characterising responses by sub-populations as well as by clones. We identify seven phenotypic subsets that, as well as sharing a conserved response to ICB, display subset-specific changes, the greatest and most divergent being within the effector cells (ECs). The T effector memory (EM) subset has been described as a crucial mediator in light of its expansion intratumorally and peripherally*(15, 28, 29)*, and we observe increases in the peripheral EM score, inferring commensurate expansion of this subset. We show though that, whilst ICB does not change EC proportion, the EC compartment exhibits the greatest magnitude of clonal and gene expression changes and preferentially persists post-ICB. As such, we posit that in peripheral blood, the effector T cell compartment is most sensitive to ICB treatment. In keeping with this, recent work shows that clones common to blood and tumour are enriched for effector markers and are not peripherally exhausted in patients who respond to ICB*(14)*.

That ICB preferentially affects large clones reveals mechanistic underpinnings to our previous observations linking large peripheral $CD8^+$ T cell clone count with clinical outcome*(18)*. Smaller clones downregulate expression of immunological pathways and increase expression of ribosomal genes and

401 translational activity post-ICB; whereas, consistent with the observation that translational suppression
402 occurs in terminal effector T cells, larger clones have an opposite response*(30)*. It is unclear to what
403 degree clonal size is a causal factor in the differential response to ICB or correlates with other factors.
404 However, that large EC clones show relative baseline upregulation of TCR signalling, likely reflective
405 of successful TCR ligation and subsequent expansion, suggests the increased sensitivity to ICB reflects
406 intrinsic activity of these clones.

407 The observation that ICB is associated with survival and expansion of clones that display markers of
408 cytotoxicity *prior* to treatment was supported by the inclusion of on treatment bulk-sequencing data
409 collated at later cycles of treatment. This highlighted that cytotoxic clones persist across multiple cycles
410 of ICB, consistent with previous descriptions of a relationship between cytotoxicity and response to
411 PD-1 blockade in the context of NSCLC*(31)*. Although it is difficult to definitively prove that ICB
412 specifically elicits clonal survival, we find that ICB does lead to increased clonal cytotoxicity. Given
413 persistent clones and expanding clones demonstrate higher cytotoxicity pre-treatment or at C2, these
414 data support this to be an action of ICB peripherally. This potentially also implies limits to patient
415 response to ICB centre on deficient tumour immunogenicity or antigen presentation, with consequential
416 limited effector T cell responses*(32)*. Thus therapies targeted at overcoming further immune
417 checkpoints may have relatively diminished clinical returns compared to those improving antigen
418 presentation and priming.

419 Consistent with the literature, we find that ICB provides a marked stimulus to mitotic cell division in
420 $CD8^+$ T cells. The relevance of this response to outcome is less clear however. Notably, the Mitotic
421 subset showed increased expression of exhaustion markers, and most mitotic clones did not appear to
422 become established at C2 or at later timepoints, with only a small proportion of surveyed mitotic $CD8^+$
423 T cells progressing to EC and EM cells. Whilst this implies dysfunction, whether these are classically
424 exhausted or are in state with features of exhaustion is unclear and will form the basis for future
425 research. Conversely, we observe that ECs remain persistently expanded for long durations, and our
426 work suggests Killer-Lectin Receptors may specifically denote long-lived ECs.

427 From a clinical outcome perspective, our work further demonstrates that analysis of peripheral $CD8^+$ T
428 cells both prior to and during treatment provides prognostic information. The association of large clone
429 count with response to ICB likely reflects the increased probability an individual will carry tumour
430 reactive clones as this count rises. Nonetheless, a situation where a few specific anti-cancer clones are
431 present could be envisaged to be beneficial, but not register in total large clone count. These cells would
432 anticipated to be cytotoxic though and here we show that a high cytotoxicity score may compensate for
433 low large clone count. Comparison of data from healthy individuals indicates that, not only do healthy
434 individuals have fewer large circulating clones, but they have diminished cytotoxicity. Finally we find
435 no association between the magnitude of the mitotic response and clinical outcome, highlighting a
436 disconnect between mitotic responses and those that are cytotoxic and therapeutically important.

437 A key question has been how these peripheral clones may relate to tumour - are they bystanders or is
438 there evidence of enrichment with those that react to melanoma antigens? By integration of our results
439 with TCR sequencing of melanoma resident T cells from Pruessman and colleagues*(26)* we demonstrate
440 that public clones found in melanomas are predominantly large, and that such reactive clones show
441 higher than average cytotoxicity. Conversely, although clones carrying TCR reactive to viral antigens
442 are plentiful, they are not larger or more cytotoxic. These findings are consistent with recent descriptions
443 of tumour-infiltrating clones which tend to have an effector-like phenotype in the peripheral blood in
444 mouse models*(17)* and patients with MM*(16)*.

445 A potential limitation of this study is the inability to definitively causally link the changes observed to
446 ICB exposure - and exclude for example effects of cancer progression or other temporal factors. This
447 is a draw-back of this type of observational work in humans – it is difficult (and ethically challenging)
448 to obtain samples from untreated individuals with cancer over time. Nonetheless, the changes we
449 observe in patient profiles coupled to the frequently pronounced transformations in clinical performance
450 strongly argue that these are due to the effect of ICB. This is underlined by bulk RNAseq data where
451 we observe a greater magnitude of change in cytotoxicity score induced by cICB versus sICB (**fig. S5c**),
452 consistent with an effect of ICB on cytotoxicity. Further, baseline cytotoxicity is higher in melanoma
453 patients than healthy volunteers, and is higher in those that respond to treatment compared to those that

454 do not (**fig. 5a**), suggesting an important interaction between baseline immune state, the effect of ICB
455 on cytotoxicity and response to treatment.

456 In summary, our work combines in-depth analysis of peripheral $CD8^+$ T cells responses to ICB at the
457 single-cell level, with observations corroborated and extended in a large dataset. The use of V(D)J
458 sequencing allows us to track clones over time, determining that most mitotic cells fail to expand into
459 differentiated large effector clones. Instead, clone size plays a key role in determining the magnitude
460 and nature of response to ICB, and we find the effector subset is most sensitive to treatment. Finally,
461 we reveal that cytotoxic clones have successfully expanded to form persistent subsets – and that much
462 of the effect of ICB appears to rely upon this pre-existent response, implicating failure of immune
463 recognition as being the major limiter of response to ICB. Going forward, efforts to understand the
464 durability and maintenance of tumour reactive clones over time will be important. Similarly,
465 understanding the degree to which other, potentially modifiable, non-tumour related factors impact on
466 the ICB response to cancer will be vital in further improving therapeutic outcomes.

467

468 **MATERIALS AND METHODS**

469 **Study design**

470 The aim of this study was to understand peripheral $CD8^+$ T cell responses to ICB at a single-cell level,
471 in particular, identifying key phenotypic or clonal features of response to therapy. Eight patients who
472 were prescribed ICB for MM at a tertiary Cancer Centre in the UK were prospectively and sequentially
473 recruited. Four participants received single agent Pembrolizumab (sICB) whilst four received
474 combination Ipilimumab/Nivolumab (cICB). Characteristics of the participants are outlined in **table S1.**
475 All participants provided written informed consent to donate samples to the Oxford Radcliffe Biobank
476 (Oxford Centre for Histopathology Research ethical approval nos. 16/A019, 18/A064, 19/A114). 30 –
477 50 ml blood was collected into EDTA tubes (BD vacutainer system) taken immediately pre-treatment
478 at d0 and d21 following one cycle of treatment (**fig. 1a**). Following single cell isolation, transcriptome
479 and V(D)J sequencing was undertaken with downstream analysis performed in R, as detailed below.

480 **Sample collection**

481 Peripheral blood mononuclear cells were immediately obtained from whole blood by density
482 centrifugation (Ficoll Paque). $CD8^+$ cell isolation was carried out by positive selection (Miltenyi)
483 according to the manufacturer's instructions, with all steps performed either at 4 °C or on ice. Unless
484 otherwise stated, patients receiving cICB (ipilimumab plus nivolumab, n=4) or sICB (pembrolizumab,
485 n=4) were pooled for the purposes of analysis, based on previous work showing qualitatively similar
486 genetic changes induced in peripheral $CD8^+$ T cells by both cICB and sICB*(18)*.

487 **Single-cell sample preparation and sequencing**

488 Magnetically separated $CD8^+$ cells were immediately oil-partitioned into single-cell droplets, followed
489 by cell lysis and a reverse transcription reaction using the 10x Genomics Chromium system. 6000 $CD8^+$
490 T cells were loaded onto each partitioning cassette. Single-cell 5' RNA transcriptome and V(D)J
491 Libraries were constructed from the cDNA, according to the manufacturer's instructions
492 (https://www.10xgenomics.com/). Due to the sequential and prospective nature of sample collection,
493 droplet generation and RT steps were performed on individual samples, but library generation and
494 sequencing was performed in two batches of pooled samples (table S1). Sequencing was performed on
495 an Illumina HiSeq4000; 75bp PE reads for the 5' RNA libraries, 150 bp PE reads for the V(D)J libraries
496 to a depth of approximately 50000 reads per cell.

497 **Data processing, quality control and clustering**

498 Single-cell reads were aligned, counted and filtered for initial quality control (QC) as previously
499 described*(12)*. In short, FASTQ files were generated from Illumina BCL outputs, used to produce gene
500 expression and barcoding libraries, and then combined using the Cellranger *mkfastq*, *count* and *aggr*
501 functions respectively. For V(D)J data, Cellranger *vdj* was applied. For QC, the R package *scater(33)*
502 was used to identify single-cell outliers as low-quality libraries and *scran* utilised to detect doublets
503 which were removed from analysis. Following alignment and data pre-processing, $CD8^+$ T cells were
504 filtered on detectable *CD3D* and either *CD8A* or *CD8B* UMIs whilst lacking *CD14* expression. The R
505 package *Seurat(34)* was used for further QC, data normalisation and identification of variable features;

low quality cells were excluded if they had less than 500 total UMIs, less than 300 detected features and mitochondrial gene percentage above 20%. Genes expressed in <5 cells were also removed. The percentage of mitochondrial genes and cell cycle scores were regressed out upon scaling of the normalised data. Principal component analysis (PCA) was performed on the scaled data and the top 16 principal components selected for dimensionality reduction and UMAP clustering as the most variable and biologically informative components. To determine an ideal resolution value, cell clusters generated using values between 0.1 and 2.5 were compared using the R package *clustree(35)* with values between 1.5 and 2.0 showing high cluster stability. Batch was not observed to have impact on Principal Component distribution and there was no significant difference in baseline cytotoxicity score between batches.*(13)*. In short, FASTQ files were generated from Illumina BCL outputs, used to produce gene expression and barcoding libraries, and then combined using the Cellranger *mkfastq*, *count* and *aggr* functions respectively. For V(D)J data, Cellranger *vdj* was applied. For QC, the R package *scater(33)* was used to identify single-cell outliers as low-quality libraries and *scran* utilised to detect doublets which were removed from analysis. Following alignment and data pre-processing, $CD8^+$ T cells were filtered on detectable *CD3D* and either *CD8A* or *CD8B* UMIs whilst lacking *CD14* expression. The R package *Seurat(34)* was used for further QC, data normalisation and identification of variable features; low quality cells were excluded if they had less than 500 total UMIs, less than 300 detected features and mitochondrial gene percentage above 20%. Genes expressed in <5 cells were also removed. The percentage of mitochondrial genes and cell cycle scores were regressed out upon scaling of the normalised data. Principal component analysis (PCA) was performed on the scaled data and the top 16 principal components selected for dimensionality reduction and UMAP clustering as the most variable and biologically informative components. To determine an ideal resolution value, cell clusters generated using values between 0.1 and 2.5 were compared using the R package *clustree(35)* with values between 1.5 and 2.0 showing high cluster stability. There was no observed effect of batch on PC distribution or baseline cytotoxicity score.

Identification of cell subsets

532 To assign each cell cluster generated in Seurat to a functional T cell subset, we curated transcripts per
533 million (TPM) normalised counts for $CD8^+$ T cells from previous T cell cancer scRNA-seq datasets*(12,*
534 *13, 36–38)*. Using the R package *SingleR(39)*, each individual cell was matched to one of the $CD8^+$ T
535 cell subsets present in the reference datasets based on global gene expression similarity, from which
536 subset identity for each cluster was determined. Briefly, we noted cluster 12 (ECs) was grouped above
537 the Mitotic clusters despite being labelled as EC through *SingleR* and having high expression of
538 FGFBP2 and other EC-characteristic genes; we detected a high level of expression of ribosomal genes
539 in this subset relative to other ECs, explaining its projection on the UMAP despite being an EC
540 cluster.*(13, 14, 39–41)*. Using the R package *SingleR(39)*, each individual cell was matched to one of
541 the $CD8^+$ T cell subsets present in the reference datasets based on global gene expression similarity,
542 from which subset identity for each cluster was determined.

543 **Clonal definitions, size and emergence vs involution**

544 T cell chains were filtered based on called productivity, and chain identity (TRA or TRB). Cells were
545 selected as those that either contained a single TCRβ chain, a combination of one TCRα with one TCRβ
546 chain or a group of three chains – two TCRα and TCRβ. Cells not meeting this criteria were excluded.
547 A clone ID was defined by a concatenation of amino acid CDR3 chains present, with cells sharing
548 identical clone IDs classed as members of the same clonotype. Clonal proportions were calculated by
549 dividing the number of cells in each clone per sample by the total of number of cells (meeting the above
550 criteria) per sample. Out of 22446 cells which had transcriptome sequencing that had passed QC, 17909
551 had matching V(D)J sequencing with required chain combinations as specified above, with these cells
552 used for all clonal analyses.

553 For analyses examining subset phenotype of clones in terms of size and evolution (e.g., **fig. 2e, S2f**),
554 cells were grouped by clone ID, individual and timepoint, and proportion of its member cells within
555 each subset was calculated; the highest proportion subset was used to describe the clone's major subset.
556 For global overview of clonal size at C1/C2 within each subset, clonal size was defined depending on

557 the timepoint the clone was sampled at. Analysis of changes in subset identity per clone (**fig. 2d**) utilised
558 clones present at both timepoints only.

559 For analyses looking at clonal changes across timepoints, only clones present at both timepoints were
560 included (e.g., **fig. 3d-g**). In this context, the size of the clone was defined based on its C1 (pre-
561 treatment) size. For clones that are present at only one timepoint (e.g., **fig. 4a**), the clone size was
562 defined based on its size when present. Similarly for analyses only at one timepoint (e.g., **fig. 4c-g, 5f-**
563 **h**) clonal size was defined based on size at that timepoint.

564 For the analysis of expanding/stable versus involuting clones between C1 and C2, only clones with >1
565 member cell were included and only cells present at C1 were analysed (**fig. 4c**). For clones that were
566 found at both timepoints, clones were designated to be involuting if the proportion at C2 was
567 significantly (a nominal p value <0.05, Fisher's exact test) smaller than the proportion at C1 and vice
568 versa for expanding. All clones that were found at C1 (with >1 member cell) but not found at C2 were
569 also classed as involuting. Expanding cells were grouped with those in which there was no significant
570 difference between timepoints (p>0.05, Fisher's exact test) as the 'stable or expanding' subset. We also
571 performed an additional analysis where clones were classified as involuting based on a range of fold
572 changes to size (**fig. S4b**). Here, 'involuting' clones were defined as those where the proportion at C2
573 was either <0.6x or <0.4x the proportion at C1 and 'stable or expanding' clones were all others.

574 For the analysis of expanding/stable versus involuting clones between C2 and C4+, again only clones
575 with >1 member cell were included and only clones present at C2 were analysed. Clones present at C4+
576 were identified based on the presence of the TCRB amino acid sequence within bulk RNAseq data of
577 magnetically sorted $CD8^+$ T cells for six of the same individuals. A clone was designated as being
578 present at C2 and C4+ if that same TCRB was found at both timepoints (C2 in scRNA-seq, C4+ in bulk
579 RNAseq). The clonal size (as a proportion) at C4+ was calculated by diving the number of reads for
580 that TCRB by the total number of TCR reads in the sample. The designation of a clone into involution
581 or expanding/stable followed the same methodology as described above, including a sensitivity analysis
582 using FC cut-offs.

583 **Downstream expression analysis**

584 ***Differential gene expression analysis with subsampling.*** Differential gene expression was performed
585 in *Seurat* using the FindMarkers function for all genes present, unless otherwise indicated.
586 Alternatively, to validate the FindMarkers results, a mixed linear model for all genes with variance >0
587 in the subsampled cells was used, controlling for interindividual variation (**fig. S3a, d**). Where specified,
588 to control for differences in statistical power in detecting DE genes across groups with varying cell
589 counts, the number of cells used for analysis was standardised to the number present in the smallest
590 group and bootstrapped 100 times to account for sampling bias. For comparison of DE genes according
591 to subset or clone size, 1100 or 245 cells were subsampled respectively as the minimum number of cells
592 across each category at both timepoints. This same methodology was repeated filtering for only ECs or
593 EMs with cells grouped into large and small clones based on a 0.5% of repertoire cut-off and
594 subsampling performed to the smallest group size.

595 ***Pathway analysis.*** Pathway enrichment analysis was performed using the R package *XGR(40)* with the
596 GOBP database. Significantly induced or suppressed genes were assessed separately against a
597 background of all detected genes using a hypergeometric test, ontology algorithm specified as
598 'elimination' and an elimination p value of 0.01. For comparisons of pathways modulated following
599 ICB across subsets, pathways were assessed for DE gene from each subsample at n=1100 cells, and the
600 frequency of enriched pathways was used for comparison; with this approach employed to maximise
601 the number of DE genes/statistical power taken forward for pathway analysis in most subsets given the
602 paucity of DE genes in Naive cells. For comparisons of pathways modulated following ICB in large
603 versus small ECs/EMs, we included the minimum number of significant DE genes across all
604 comparators, keeping the number of genes used in the analysis constant between groups.

605 ***Leave-one-out cross validation.*** In order to explore the effect of inter-individual variation, we repeated
606 the differential gene expression with subsampling analysis eight times, with all cells from one individual
607 excluded each time. This demonstrated consistency in results suggesting that the observed effect is not
608 driven solely by cells from one donor.

609 ***Generation of cytotoxicity score.*** Cell scores for cytotoxicity were calculated using AddModuleScore
610 in Seurat, based on the top 50 variable feature genes that significantly correlated with *IFNG* expression
611 *(41)* (see supplementary data file 2). For PDCD1 and TIGIT expression analysis, the MAGIC R package
612 was used to recover expression data*(42).* In most instances – and as indicated in the figures and figure
613 legends – cytotoxicity score is reported on a clonal basis. Here, cells were grouped for each individual
614 and timepoint based on clone ID and the cytotoxicity score calculated as a median of the cytotoxicity
615 scores for all cells within that clone.

616 **Bulk RNA-sequencing**

617 Bulk RNA-sequencing was performed on $CD8^+$ T cells from 69 healthy individuals and 140 patients
618 receiving single or combination ICB for MM, with exclusion of adjuvant treated patients. Out of 137
619 C1 and 113 C2 samples, 110 individuals had paired C1/C2 data with a further 49 having C4 samples.
620 Clinical follow-up was available for 132 C1 and 109 C2 samples. Gene expression and TCR analysis
621 using the MiXCR package was performed as previously described; for full methods, please see*(18)*.
622 Data can be downloaded from the European Bioinformatics Institute and the Centre for Genomic
623 Regulation under accession no. EGAS00001004081.

624 To generate subset scores from each bulk sample, hallmark genes for each subset were identified in the
625 single-cell data using the FindAllMarkers function in Seurat across all cells from C1 and C2 samples
626 separately. To minimise timepoint-specific genes, the top 20 genes at each timepoint were selected and
627 the overlapping genes retained as robust subset-demarcating genes (**table S2**). Scores were then
628 generated for each gene-set using *DESeq2*-normalised expression data *(43)* to then calculate geometric
629 mean expression for each group of subset genes. A similar approach was used for cytotoxic score but
630 instead based on the top 50 genes used for single-cell cytotoxic scoring. All metadata is listed in **table**
631 **S11**.

632 For clonal persistence at C4+, we used longitudinal bulk samples from six individuals for which single-
633 cell data was obtained; four taken at day 63, one at day 84 and one at day 106 of treatment. Clones were

634 defined within these samples using MiXCR *(44)* according to the beta chain, and then compared with
635 earlier scRNA-seq data with matching beta chain usage.

636 **Flow cytometry**

637 Patient PBMCs frozen in 90% FCS + 10% DMSO were thawed at 37°C and washed once in HBSS
638 prior to staining of $1x10^6$ cells with LIVE/DEAD Fixable Near-IR (Invitrogen). Cells were washed and
639 subsequently stained with antibodies against CD3, CD8, CD16, CD56, CD45RA, CD27, CX3CR1 and
640 HLA-DR in 5% FBS + HBSS. After washing, cells were fixed for 10 minutes with 2%
641 paraformaldehyde (Sigma), washed and then permeabilised with 1x Permeabilisation Buffer
642 (eBioscience) for 10 minutes. The cells were then stained with Perforin-1, CCL4, Granzyme-B, IFN-g,
643 TNF-a, IL-32 and Granulysin, washed with perm buffer and stained with anti-rat IgG2a secondary ,
644 before a final wash with perm buffer and acquisition on a BD LSRFortessa X-20. Data was analysed in
645 FlowJo (FlowJo LLC). Antibodies details are shown in **table S9** and gating is outlined in **table S10**.
646 All staining steps were performed for 30 minutes and at 4°C unless otherwise stated.

647 **Analysis of external datasets**

648 Melanoma tumour TCRB-seq and FKPM-normalised RNA-seq from Riaz et al. 2017 *(25)* were
649 downloaded from https://github.com/riazn/bms038_analysis or from GEO:GSE91061 respectively. To
650 generate an intratumoral cytotoxicity score, the 50 genes used for single-cell cytotoxic scoring were
651 correlated against the expression of *CD3D*, *CD3E*, *CD8A*, *CD8B*, *IFNG* and *PRF1* and k-means
652 clustered to identify a module of genes most associated with $CD8^+$ T cell cytotoxicity. Geometric mean
653 expression of the eight genes was then calculated per sample and used as cytotoxic score. Large clone
654 count per TCRB sample was calculated as for the bulk CD8 sequencing data (i.e., the number of clones
655 occupying greater than 0.5% of the repertoire). Survival analysis was conducted for the 52 samples with
656 overlapping RNA-seq and TCRB data (26 pre-treatment, 26 on-treatment) (**table S12**). Analysis of
657 public melanoma and viral T cell clones was done using TCRB-seq data of 199 melanomas from
658 Pruessman et al. 2020 *(26)*, or viral-reactive TCR sequences downloaded from VDJdb *(27, 45)*
659 [04/2021] with confidence scores above 0. Cells present in the scRNA-seq data were annotated as being

660 found in melanoma or viral-reactive based on their ownership of a TCRB that was found in either the
661 Pruessman or VDJdb dataset.

662 **General statistical analysis**

663 Statistical comparisons were performed as indicated in each figure and conducted in R. Paired tests
664 were used for paired samples. Cells and statistics from donor 6 were excluded from all analyses in figure
665 2c-d, S2e and figure 4 due to low numbers of cells at C1. For analysis of clonal persistence (**fig. 4d-g**),
666 n=6 as only six out of the eight individuals profiled had samples at C4+. All analyses and statistical
667 tests were performed in R using baseR or *rstatix,* and *lme4*/*lmerTest* for linear effect models. LDA
668 analysis was performed using *MASS* and *Pi (46)*. Gene correlation analysis for phenotype scores was
669 performed using *DGCA(47)*. Survival analysis was performed using *survival*/*survminer*. *UpSetR(48)*
670 *networkD3* and *ComplexHeatmap(49)* were used for visualisation. For all data, *p<0.05, **p<0.01,
671 ***p< 0.001, ****p<0.0001. Adjusted p-values have been reported using Bonferroni correction for
672 multiple comparisons.

673

674 **LIST OF SUPPLEMENTARY MATERIALS**

675 Supplementary tables are found in excel workbook as separate tabs
676 S1: Single Cell Characteristics
677 S2: Subset Scoring
678 S3: Cytotoxic Scoring
679 S4: TCR information
680 S5: Movement of clonal subsets
681 S6: Subset DEGs
682 S7: Subset + clone DEGs
683 S8: Stable vs involuting clone markers
684 S9: Flow Cytometry Antibodies
685 S10: Flow Cytometry gating
686 S11: Bulk RNAseq Metadata
687 S12: Riaz et al. Analysis
688

689 **REFERENCES**

690 1. M. A. Postow, M. K. Callahan, J. D. Wolchok, Immune Checkpoint Blockade in Cancer Therapy.,
691 *Journal of clinical oncology : official journal of the American Society of Clinical Oncology* **33**, 1974–82
692 (2015).

693 2. J. Larkin, V. Chiarion-Sileni, R. Gonzalez, J.-J. Grob, P. Rutkowski, C. D. Lao, C. L. Cowey, D.
694 Schadendorf, J. Wagstaff, R. Dummer, P. F. Ferrucci, M. Smylie, D. Hogg, A. Hill, I. Márquez-Rodas, J.
695 Haanen, M. Guidoboni, M. Maio, P. Schöffski, M. S. Carlino, C. Lebbé, G. McArthur, P. A. Ascierto, G.
696 A. Daniels, G. v. Long, L. Bastholt, J. I. Rizzo, A. Balogh, A. Moshyk, F. S. Hodi, J. D. Wolchok, Five-Year
697 Survival with Combined Nivolumab and Ipilimumab in Advanced Melanoma, *New England Journal of*
698 *Medicine* **381**, 1535–1546 (2019).

699 3. A. M. Goodman, S. Kato, L. Bazhenova, S. P. Patel, G. M. Frampton, V. Miller, P. J. Stephens, G. A.
700 Daniels, R. Kurzrock, Tumor mutational burden as an independent predictor of response to
701 immunotherapy in diverse cancers, *Molecular Cancer Therapeutics* **16**, 2598–2608 (2017).

702 4. J. Y. Kim, A. Kronbichler, M. Eisenhut, S. H. Hong, H. J. van der Vliet, J. Kang, J. il Shin, G. Gamerith,
703 Tumor mutational burden and efficacy of immune checkpoint inhibitors: A systematic review and
704 meta-analysis, *Cancers* **11**, 11 (2019).

705 5. T. A. Chan, M. Yarchoan, E. Jaffee, C. Swanton, S. A. Quezada, A. Stenzinger, S. Peters,
706 Development of tumor mutation burden as an immunotherapy biomarker: Utility for the oncology
707 clinic*Annals of Oncology* **30**, 44–56 (2019).

708 6. T. A. Barnes, E. Amir, HYPE or HOPE: The prognostic value of infiltrating immune cells in
709 cancer*British Journal of Cancer* **117**, 451–460 (2017).

710 7. F. Maibach, H. Sadozai, S. M. Seyed Jafari, R. E. Hunger, M. Schenk, Tumor-Infiltrating
711 Lymphocytes and Their Prognostic Value in Cutaneous Melanoma*Frontiers in Immunology* **11** (2020),
712 doi:10.3389/fimmu.2020.02105.

713 8. A. C. Huang, M. A. Postow, R. J. Orlowski, R. Mick, B. Bengsch, S. Manne, W. Xu, S. Harmon, J. R.
714 Giles, B. Wenz, M. Adamow, D. Kuk, K. S. Panageas, C. Carrera, P. Wong, F. Quagliarello, B.
715 Wubbenhorst, K. D'Andrea, K. E. Pauken, R. S. Herati, R. P. Staupe, J. M. Schenkel, S. McGettigan, S.
716 Kothari, S. M. George, R. H. Vonderheide, R. K. Amaravadi, G. C. Karakousis, L. M. Schuchter, X. Xu, K.
717 L. Nathanson, J. D. Wolchok, T. C. Gangadhar, E. J. Wherry, T-cell invigoration to tumour burden ratio
718 associated with anti-PD-1 response, *Nature* **545**, 60–65 (2017).

719 9. A. D. Waldman, J. M. Fritz, M. J. Lenardo, A guide to cancer immunotherapy: from T cell basic
720 science to clinical practice*Nature Reviews Immunology* **20**, 651–668 (2020).

721 10. N. E. Thomas, K. J. Busam, L. From, A. Kricker, B. K. Armstrong, H. Anton-Culver, S. B. Gruber, R. P.
722 Gallagher, R. Zanetti, S. Rosso, T. Dwyer, A. Venn, P. A. Kanetsky, P. A. Groben, H. Hao, I. Orlow, A. S.
723 Reiner, L. Luo, S. Paine, D. W. Ollila, H. Wilcox, C. B. Begg, M. Berwick, Tumor-infiltrating lymphocyte
724 grade in primary melanomas is independently associated with melanoma-specific survival in the
725 population-based genes, environment and melanoma study, *Journal of Clinical Oncology* **31**, 4252–
726 4259 (2013).

727 11. P. C. Tumeh, C. L. Harview, J. H. Yearley, I. P. Shintaku, E. J. M. Taylor, L. Robert, B. Chmielowski,
728 M. Spasic, G. Henry, V. Ciobanu, A. N. West, M. Carmona, C. Kivork, E. Seja, G. Cherry, A. J. Gutierrez,
729 T. R. Grogan, C. Mateus, G. Tomasic, J. A. Glaspy, R. O. Emerson, H. Robins, R. H. Pierce, D. A.

730 Elashoff, C. Robert, A. Ribas, PD-1 blockade induces responses by inhibiting adaptive immune
731 resistance., *Nature* **515**, 568–71 (2014).

732 12. K. E. Yost, A. T. Satpathy, D. K. Wells, Y. Qi, C. Wang, R. Kageyama, K. L. McNamara, J. M. Granja,
733 K. Y. Sarin, R. A. Brown, R. K. Gupta, C. Curtis, S. L. Bucktrout, M. M. Davis, A. L. S. Chang, H. Y. Chang,
734 Clonal replacement of tumor-specific T cells following PD-1 blockade, *Nature Medicine* **25**, 1251–
735 1259 (2019).

736 13. T. D. Wu, S. Madireddi, P. E. de Almeida, R. Banchereau, Y. J. J. Chen, A. S. Chitre, E. Y. Chiang, H.
737 Iftikhar, W. E. O'Gorman, A. Au-Yeung, C. Takahashi, L. D. Goldstein, C. Poon, S. Keerthivasan, D. E.
738 de Almeida Nagata, X. Du, H. M. Lee, K. L. Banta, S. Mariathasan, M. das Thakur, M. A. Huseni, M.
739 Ballinger, I. Estay, P. Caplazi, Z. Modrusan, L. Delamarre, I. Mellman, R. Bourgon, J. L. Grogan,
740 Peripheral T cell expansion predicts tumour infiltration and clinical response, *Nature* **579**, 274–278
741 (2020).

742 14. L. Lucca, P.-P. Axisa, B. Lu, B. Harnett, S. Jessel, L. Zhang, K. Raddassi, L. Zhang, K. Olino, J. Clune,
743 M. Singer, D. A. Hafler, Circulating Clonally Expanded T Cells Reflect Functions of Tumor Infiltrating T
744 Cells 2 3 Running title 1 Single-cell RNAseq of circulating TILs in Melanoma 2 3, *bioRxiv* ,
745 2020.09.30.321240 (2020).

746 15. S. Valpione, E. Galvani, J. Tweedy, P. A. Mundra, A. Banyard, P. Middlehurst, J. Barry, S. Mills, Z.
747 Salih, J. Weightman, A. Gupta, G. Gremel, F. Baenke, N. Dhomen, P. C. Lorigan, R. Marais, Immune
748 awakening revealed by peripheral T cell dynamics after one cycle of immunotherapy, *Nature Cancer*
749 **1**, 210–221 (2020).

750 16. L. E. Lucca, P. P. Axisa, B. Lu, B. Harnett, S. Jessel, L. Zhang, K. Raddassi, L. Zhang, K. Olino, J.
751 Clune, M. Singer, H. M. Kluger, D. A. Hafler, Circulating clonally expanded T cells reflect functions of
752 tumor-infiltrating T cells, *Journal of Experimental Medicine* **218** (2021), doi:10.1084/JEM.20200921.

753 17. K. E. Pauken, O. Shahid, K. A. Lagattuta, K. M. Mahuron, J. M. Luber, M. M. Lowe, L. Huang, C.
754 Delaney, J. M. Long, M. E. Fung, K. Newcomer, K. K. Tsai, M. Chow, S. Guinn, J. R. Kuchroo, K. P.
755 Burke, J. M. Schenkel, M. D. Rosenblum, A. I. Daud, A. H. Sharpe, M. Singer, Single-cell analyses
756 identify circulating anti-tumor CD8 T cells and markers for their enrichment, *Journal of Experimental*
757 *Medicine* **218** (2021), doi:10.1084/JEM.20200920.

758 18. B. P. Fairfax, C. A. Taylor, R. A. Watson, I. Nassiri, S. Danielli, H. Fang, E. A. Mahé, R. Cooper, V.
759 Woodcock, Z. Traill, M. H. Al-Mossawi, J. C. Knight, P. Klenerman, M. Payne, M. R. Middleton,
760 Peripheral $CD8^+$ T cell characteristics associated with durable responses to immune checkpoint
761 blockade in patients with metastatic melanoma, *Nature Medicine* **26** (2020), doi:10.1038/s41591-
762 019-0734-6.

763 19. K. H. Kim, J. Cho, B. M. Ku, J. Koh, J. M. Sun, S. H. Lee, J. S. Ahn, J. Cheon, Y. J. Min, S. H. Park, K.
764 Park, M. J. Ahn, E. C. Shin, The first-week proliferative response of peripheral blood PD-1þCD8þ T
765 cells predicts the response to Anti-PD-1 therapy in solid tumors, *Clinical Cancer Research* **25**, 2144–
766 2154 (2019).

767 20. M. Ayers, J. Lunceford, M. Nebozhyn, E. Murphy, A. Loboda, D. R. Kaufman, A. Albright, J. D.
768 Cheng, S. P. Kang, V. Shankaran, S. A. Piha-Paul, J. Yearley, T. Y. Seiwert, A. Ribas, T. K. McClanahan,
769 IFN-γ-related mRNA profile predicts clinical response to PD-1 blockade, *Journal of Clinical*
770 *Investigation* **127**, 2930–2940 (2017).

771 21. P. A. Szabo, H. M. Levitin, M. Miron, M. E. Snyder, T. Senda, J. Yuan, Y. L. Cheng, E. C. Bush, P.
772 Dogra, P. Thapa, D. L. Farber, P. A. Sims, Single-cell transcriptomics of human T cells reveals tissue
773 and activation signatures in health and disease, *Nature Communications* **10**, 1–16 (2019).

774 22. G. X. Y. Zheng, J. M. Terry, P. Belgrader, P. Ryvkin, Z. W. Bent, R. Wilson, S. B. Ziraldo, T. D.
775 Wheeler, G. P. McDermott, J. Zhu, M. T. Gregory, J. Shuga, L. Montesclaros, J. G. Underwood, D. A.
776 Masquelier, S. Y. Nishimura, M. Schnall-Levin, P. W. Wyatt, C. M. Hindson, R. Bharadwaj, A. Wong, K.
777 D. Ness, L. W. Beppu, H. J. Deeg, C. McFarland, K. R. Loeb, W. J. Valente, N. G. Ericson, E. A. Stevens,
778 J. P. Radich, T. S. Mikkelsen, B. J. Hindson, J. H. Bielas, Massively parallel digital transcriptional
779 profiling of single cells, *Nature Communications* **8** (2017), doi:10.1038/ncomms14049.

780 23. G. Pizzolato, H. Kaminski, M. Tosolini, D. M. Franchini, F. Pont, F. Martins, C. Valle, D.
781 Labourdette, S. Cadot, A. Quillet-Mary, M. Poupot, C. Laurent, L. Ysebaert, S. Meraviglia, F. Dieli, P.
782 Merville, P. Milpied, J. Déchanet-Merville, J. J. Fournié, Single-cell RNA sequencing unveils the shared
783 and the distinct cytotoxic hallmarks of human TCRVδ1 and TCRVδ2 γδ T lymphocytes, *Proceedings of*
784 *the National Academy of Sciences of the United States of America* **116**, 11906–11915 (2019).

785 24. R. Aguirre-Gamboa, I. Joosten, P. C. M. Urbano, R. G. van der Molen, E. van Rijssen, B. van
786 Cranenbroek, M. Oosting, S. Smeekens, M. Jaeger, M. Zorro, S. Withoff, A. E. van Herwaarden, F. C.
787 G. J. Sweep, R. T. Netea, M. A. Swertz, L. Franke, R. J. Xavier, L. A. B. Joosten, M. G. Netea, C.
788 Wijmenga, V. Kumar, Y. Li, H. J. P. M. Koenen, Differential Effects of Environmental and Genetic
789 Factors on T and B Cell Immune Traits, *Cell Reports* **17**, 2474–2487 (2016).

790 25. N. Riaz, J. J. Havel, V. Makarov, A. Desrichard, W. J. Urba, J. S. Sims, F. S. Hodi, S. Martín-Algarra,
791 R. Mandal, W. H. Sharfman, S. Bhatia, W.-J. Hwu, T. F. Gajewski, C. L. Slingluff, D. Chowell, S. M.
792 Kendall, H. Chang, R. Shah, F. Kuo, L. G. T. Morris, J.-W. Sidhom, J. P. Schneck, C. E. Horak, N.
793 Weinhold, T. A. Chan, Tumor and Microenvironment Evolution during Immunotherapy with
794 Nivolumab, *Cell* **171**, 934-949.e15 (2017).

795 26. W. Pruessmann, J. Rytlewski, J. Wilmott, M. C. Mihm, G. H. Attrill, B. Dyring-Andersen, P. Fields,
796 Q. Zhan, A. J. Colebatch, P. M. Ferguson, J. F. Thompson, K. Kallenbach, E. Yusko, R. A. Clark, H.
797 Robins, R. A. Scolyer, T. S. Kupper, Molecular analysis of primary melanoma T cells identifies patients
798 at risk for metastatic recurrence, *Nature Cancer* **1**, 197–209 (2020).

799 27. D. v. Bagaev, R. M. A. Vroomans, J. Samir, U. Stervbo, C. Rius, G. Dolton, A. Greenshields-Watson,
800 M. Attaf, E. S. Egorov, I. v. Zvyagin, N. Babel, D. K. Cole, A. J. Godkin, A. K. Sewell, C. Kesmir, D. M.
801 Chudakov, F. Luciani, M. Shugay, VDJdb in 2019: Database extension, new analysis infrastructure and
802 a T-cell receptor motif compendium, *Nucleic Acids Research* **48**, D1057–D1062 (2020).

803 28. M. Enamorado, S. Iborra, E. Priego, F. J. Cueto, J. A. Quintana, S. Martýnez-Cano, E. Mejyás-Perez,
804 M. Esteban, I. Melero, A. Hidalgo, D. Sancho, Enhanced anti-tumour immunity requires the interplay
805 between resident and circulating memory CD8+ T cells, *Nature Communications* **8**, 1–11 (2017).

806 29. A. Ribas, D. S. Shin, J. Zaretsky, J. Frederiksen, A. Cornish, E. Avramis, E. Seja, C. Kivork, J. Siebert,
807 P. Kaplan-Lefko, X. Wang, B. Chmielowski, J. A. Glaspy, P. C. Tumeh, T. Chodon, D. Pe'er, B. Comin-
808 Anduix, PD-1 blockade expands intratumoral memory T cells, *Cancer Immunology Research* **4**, 194–
809 203 (2016).

810 30. K. Araki, M. Morita, A. G. Bederman, B. T. Konieczny, H. T. Kissick, N. Sonenberg, R. Ahmed,
811 Translation is actively regulated during the differentiation of CD8 + effector T cells, *Nature*
812 *Immunology* **18**, 1046–1057 (2017).

813 31. K. Iwahori, Y. Shintani, S. Funaki, Y. Yamamoto, M. Matsumoto, T. Yoshida, A. Morimoto-
814 Okazawa, A. Kawashima, E. Sato, S. Gottschalk, M. Okumura, A. Kumanogoh, H. Wada, Peripheral T
815 cell cytotoxicity predicts T cell function in the tumor microenvironment, *Scientific Reports* **9**, 1–12
816 (2019).

817 32. R. W. Jenkins, D. A. Barbie, K. T. Flaherty, Mechanisms of resistance to immune checkpoint
818 inhibitors, *British Journal of Cancer* **118**, 9–16 (2018).

819 33. D. J. McCarthy, K. R. Campbell, A. T. L. Lun, Q. F. Wills, Scater: Pre-processing, quality control,
820 normalization and visualization of single-cell RNA-seq data in R, *Bioinformatics* **33**, 1179–1186
821 (2017).

822 34. A. Butler, P. Hoffman, P. Smibert, E. Papalexi, R. Satija, Integrating single-cell transcriptomic data
823 across different conditions, technologies, and species, *Nature Biotechnology* **36**, 411–420 (2018).

824 35. L. Zappia, A. Oshlack, Clustering trees: a visualization for evaluating clusterings at multiple
825 resolutions, *GigaScience* **7** (2018), doi:10.1093/gigascience/giy083.

826 36. X. Guo, Y. Zhang, L. Zheng, C. Zheng, J. Song, Q. Zhang, B. Kang, Z. Liu, L. Jin, R. Xing, R. Gao, L.
827 Zhang, M. Dong, X. Hu, X. Ren, D. Kirchhoff, H. G. Roider, T. Yan, Z. Zhang, Global characterization of
828 T cells in non-small-cell lung cancer by single-cell sequencing, *Nature Medicine* **24**, 978–985 (2018).

829 37. P. Savas, B. Virassamy, C. Ye, A. Salim, C. P. Mintoff, F. Caramia, R. Salgado, D. J. Byrne, Z. L. Teo,
830 S. Dushyanthen, A. Byrne, L. Wein, S. J. Luen, C. Poliness, S. S. Nightingale, A. S. Skandarajah, D. E.
831 Gyorki, C. M. Thornton, P. A. Beavis, S. B. Fox, P. K. Darcy, T. P. Speed, L. K. MacKay, P. J. Neeson, S.
832 Loi, Single-cell profiling of breast cancer T cells reveals a tissue-resident memory subset associated
833 with improved prognosis, *Nature Medicine* **24**, 986–993 (2018).

834 38. L. Zhang, X. Yu, L. Zheng, Y. Zhang, Y. Li, Q. Fang, R. Gao, B. Kang, Q. Zhang, J. Y. Huang, H. Konno,
835 X. Guo, Y. Ye, S. Gao, S. Wang, X. Hu, X. Ren, Z. Shen, W. Ouyang, Z. Zhang, Lineage tracking reveals
836 dynamic relationships of T cells in colorectal cancer, *Nature* **564**, 268–272 (2018).

837 39. D. Aran, A. P. Looney, L. Liu, E. Wu, V. Fong, A. Hsu, S. Chak, R. P. Naikawadi, P. J. Wolters, A. R.
838 Abate, A. J. Butte, M. Bhattacharya, Reference-based analysis of lung single-cell sequencing reveals a
839 transitional profibrotic macrophage, *Nature Immunology* **20**, 163–172 (2019).

840 40. H. Fang, B. Knezevic, K. L. Burnham, J. C. Knight, XGR software for enhanced interpretation of
841 genomic summary data, illustrated by application to immunological traits, *Genome Medicine* **8**, 129
842 (2016).

843 41. S. Aibar, C. B. González-Blas, T. Moerman, V. A. Huynh-Thu, H. Imrichova, G. Hulselmans, F.
844 Rambow, J. C. Marine, P. Geurts, J. Aerts, J. van den Oord, Z. K. Atak, J. Wouters, S. Aerts, SCENIC:
845 Single-cell regulatory network inference and clustering, *Nature Methods* **14**, 1083–1086 (2017).

846 42. C. Trapnell, D. Cacchiarelli, J. Grimsby, P. Pokharel, S. Li, M. Morse, N. J. Lennon, K. J. Livak, T. S.
847 Mikkelsen, J. L. Rinn, The dynamics and regulators of cell fate decisions are revealed by
848 pseudotemporal ordering of single cells, *Nature Biotechnology* **32**, 381–386 (2014).

849 43. M. I. Love, W. Huber, S. Anders, Moderated estimation of fold change and dispersion for RNA-
850 seq data with DESeq2, *Genome Biology* **15** (2014), doi:10.1186/s13059-014-0550-8.

851 44. D. A. Bolotin, S. Poslavsky, I. Mitrophanov, M. Shugay, I. Z. Mamedov, E. v. Putintseva, D. M.
852 Chudakov, MiXCR: Software for comprehensive adaptive immunity profiling*Nature Methods* **12**,
853 380–381 (2015).

45. VDJdb (available at https://vdjdb.cdr3.net/).

46. H. Fang, G. Beckmann, C. Bountra, P. Bowness, N. Burgess-Brown, L. Carpenter, L. Chen, D. Damerell, U. Egner, H. Fang, R. Fujii, T. Howe, P. J. Jakobsson, A. Katopodis, J. C. Knight, B. D. Marsden, J. de Martino, G. Matthias, G. McVean, A. Mueller-Fahrnow, A. Mälarstig, C. A. O'Callaghan, N. Ostermann, J. R. Paez-cortez, P. J. Peeters, F. Prinz, P. Soulard, M. Sundström, C. Yabuki, J. Vlach, H. de Wolf, B. Knezevic, K. L. Burnham, J. Osgood, A. Sanniti, A. Lledó Lara, S. Kasela, S. de Cesco, J. K. Wegner, L. Handunnetthi, F. E. McCann, L. Chen, T. Sekine, P. E. Brennan, B. D. Marsden, D. Damerell, C. A. O'Callaghan, C. Bountra, P. Bowness, Y. Sundström, L. Milani, L. Berg, H. W. Göhlmann, P. J. Peeters, B. P. Fairfax, M. Sundström, J. C. Knight, A genetics-led approach defines the drug target landscape of 30 immune-related traits, *Nature Genetics* **51**, 1082–1091 (2019).

47. A. T. McKenzie, I. Katsyv, W. M. Song, M. Wang, B. Zhang, DGCA: A comprehensive R package for Differential Gene Correlation Analysis, *BMC Systems Biology* **10** (2016), doi:10.1186/s12918-016-0349-1.

48. J. R. Conway, A. Lex, N. Gehlenborg, UpSetR: An R package for the visualization of intersecting sets and their properties, *Bioinformatics* **33**, 2938–2940 (2017).

49. Z. Gu, R. Eils, M. Schlesner, Complex heatmaps reveal patterns and correlations in multidimensional genomic data, *Bioinformatics* **32**, 2847–2849 (2016).

874 **ACKNOWLEDGEMENTS**

875 We are very grateful to all patients who generously contributed samples and participated in the study.
876 We thank all the staff of the Day Treatment Unit, Oxford Cancer Centre, and The Brodey Centre at the
877 Horton General Hospital. We also thank M. Payne, N. Coupe and R. Matin for assistance in collecting
878 patient samples. We thank M. H. Al-Mossawi for discussion and advice.

879

880 **FUNDING**

881 This study was funded by a Wellcome Intermediate Clinical Fellowship to BPF (no. 201488/Z/16/Z),
882 additionally supporting AV, EAM and IN. RAW was a National Institute for Health Research (NIHR)
883 Academic Clinical Fellow at the time of this project, and was supported by a Cancer Research UK
884 (CRUK) predoctoral Fellowship (no. ANR00740); currently funded by a Wellcome Trust Doctoral
885 Training Fellowship (no. BST00070). OT is supported by The Clarendon Fund, St Edmund Hall, and
886 an Oxford Australia Scholarship. RC is supported by a CRUK Clinical Research Training Fellowship
887 (S_3578). CAT is funded by the Engineering & Physical Sciences Research Council and the Balliol
888 Jowett Society (no. D4T00070). HR is funded by the Medical Research Council (MRC MC UU
889 00002/10) and the Lopez-Loreta Foundation. MRM and BPF are supported by the NIHR Oxford
890 Biomedical Research Centre. The views expressed are those of the authors and not necessarily those of
891 the NHS, the NIHR or the Department of Health.

892

893 **AUTHOR CONTRIBUTIONS**

894 RAW & BPF conceived the study; RAW, OT, IN & BPF performed the analysis; figures were generated
895 by OT & RAW; manuscript was drafted by RAW, OT & BPF; RAW & RC performed single-cell
896 experiments; OT and PKS performed flow cytometry experiments; RAW, EAM, RC, CAT, PKS, AV
897 & OT collected and prepared samples; HR provided expert statistical advice; MRM contributed to

898 discussions throughout the work; BPF oversaw the project. All authors read, edited and approved the
899 final manuscript.

900

901 **COMPETING INTERESTS**

902 RAW, OT, RC, CAT, AV, PKS, EAM, HR, IN– no competing interests

903 MRM – reports grants from Roche, grants from Astrazeneca, grants and personal fees from GSK,
904 personal fees and other from Novartis, other from Millenium, personal fees and other from
905 Immunocore, personal fees and other from BMS, personal fees and other from Eisai, other from Pfizer,
906 personal fees, non-financial support and other from Merck/MSD, personal fees and other from Rigontec
907 (acquired by MSD), other from Regeneron, personal fees and other from BiolineRx, personal fees and
908 other from Array Biopharma (now Pfizer), non-financial support and other from Replimune, personal
909 fees from Kineta, personal fees from Silicon Therapeutics, outside the submitted work.

910 BPF – received conference support from BMS.

911

912 **DATA AND MATERIALS AVAILABILITY**

913 Raw expression matrices and associated cell metadata for all cells that passed upstream QC will be
914 deposited on EGA. All scripts used in data analysis and the generation of figures will be made available
915 on the Fairfax group bitbucket account.

916

917 **SUPPLEMENTARY FIGURES**

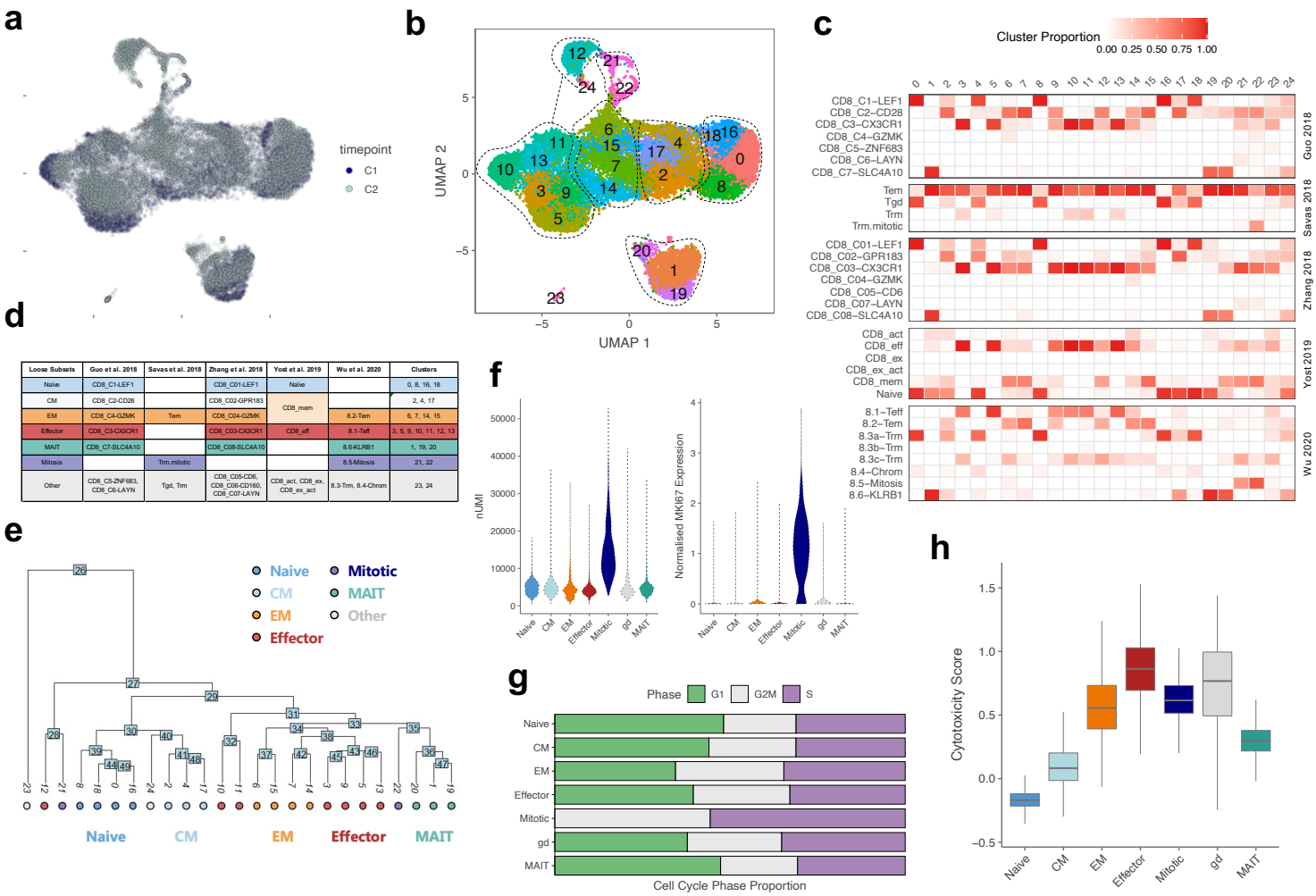

Loose Subsets	Guo et al. 2018	Savas et al. 2018	Zhang et al. 2018	Yost et al. 2019	Wu et al. 2020	Clusters
Naive	CD8_C1-LEF1		CD8_C01-LEF1	Naive		0, 8, 16, 18
CM	CD8_C2-CD28		CD8_C02-GPR183	CD8_mem		2, 4, 17
EM	CD8_C4-GZMK	Tem	CD8_C04-GZMK		8.2-Tem	6, 7, 14, 15
Effector	CD8_C3-CX3CR1		CD8_C03-CX3CR1	CD8_eff	8.1-Teff	3, 5, 9, 10, 11, 12, 13
MAIT	CD8_C7-SLC4A10		CD8_C08-SLC4A10		8.6-KLRB1	1, 19, 20
Mitosis		Trm.mitotic			8.5-Mitosis	21, 22
Other	CD8_C5-ZNF683, CD8_C6-LAYN	Tgd, Trm	CD8_C05-CD6, CD8_C06-CD160, CD8_C07-LAYN	CD8_act, CD8_ex, CD8_ex_act	8.3-Trm, 8.4-Chrom	23, 24

918

919 **Supplementary Figure 1**: **Workflow for CD8$^+$ T cell subset assignments. (a)** UMAP distribution of
920 cells from pre-treatment (C1) and day 21 on-treatment (C2) samples. **(b)** UMAP visualisation of 25
921 Seurat clusters generated at a FindClusters resolution of 1.5. **(c)** Heatmap of assigned subset identities
922 for each Seurat cluster using external cancer patient single-cell RNAseq datasets as a reference*(12, 13,*
923 *36–38)* . For each cell, SingleR was used to cross-match its expression profile to that of one of the
924 subsets in each reference set. The proportion of cells in each cluster that were assigned a particular
925 identity from each reference set is represented by the intensity of shading (between 0 and 1). **(d)**
926 Summary table of subset identities for each reference set and assigned identities for each cluster based
927 on the best match from the SingleR analysis. **(e)** Phylogenetic tree for each Seurat cluster coloured by
928 assigned subset showing similarity between clusters within the same subset. **(f)** Violin plot showing the
929 nUMI (left) and normalised MKI67 expression (right) per cell across each of the seven CD8$^+$ T cell
930 subsets. **(g)** Bar plot of the proportion of cells in each stage of the cell cycle, assigned using the
931 CellCycleScoring function in Seurat, across each subset. **(h)** Cytotoxicity score (based on expression of
932 the 50 most *IFNG*-correlating genes, Supplementary Table S3) across each subset.

933

934

935

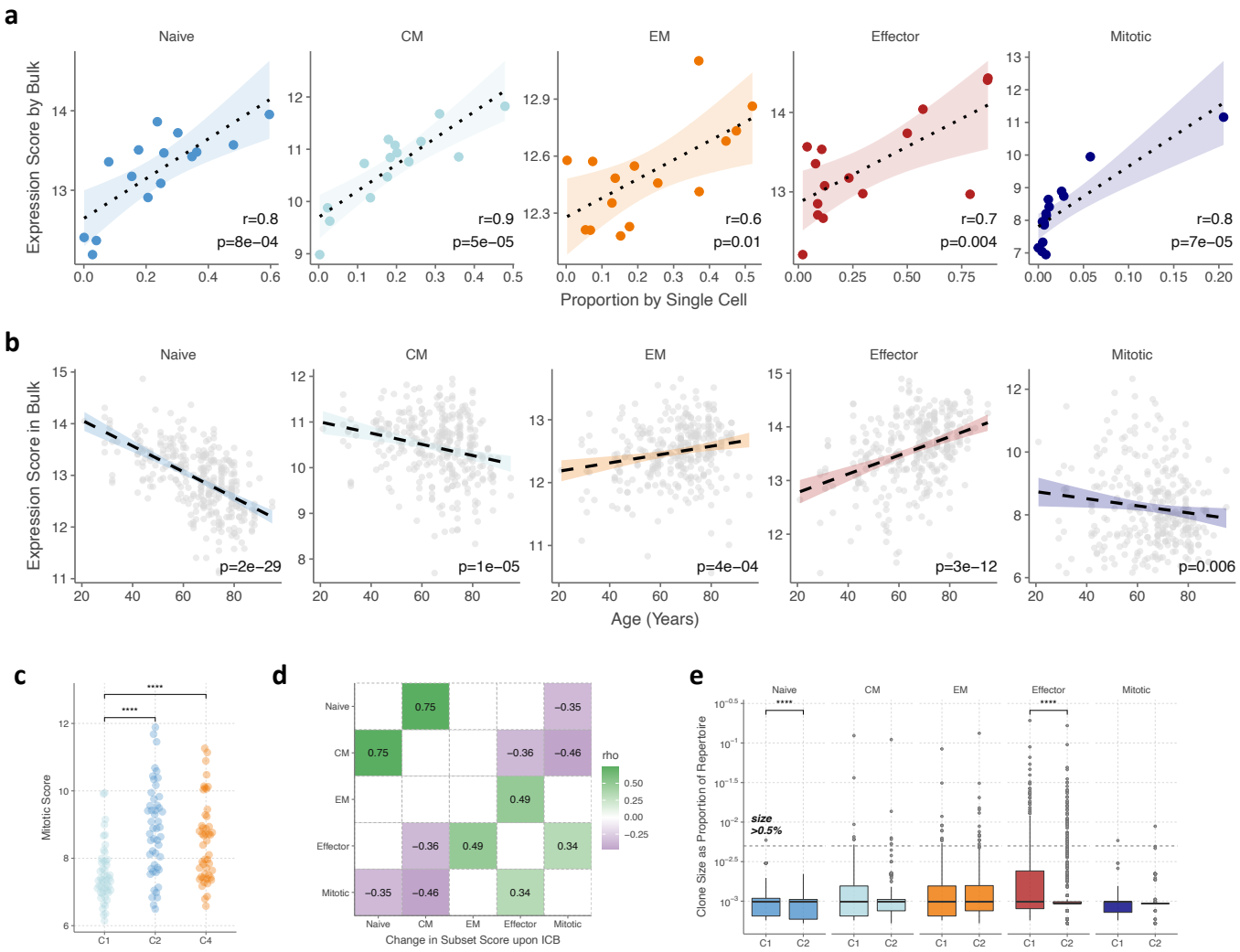

936 **Supplementary Figure 2**: **Inference of subset proportions and phenotype. (a)** Correlation between
937 subset proportions for each single-cell sample and scores calculated for each subset using bulk RNAseq
938 data of $CD8^+$ T cells. For 15/16 of the samples used for single-cell RNAseq, bulk RNAseq on the
939 purified $CD8^+$ T cells was also performed. A list of the top 20 discriminating markers for each subset
940 was generated using FindAllMarkers in the single-cell data for all pre-treatment cells, and separately
941 for all cells at d21 post-ICB. The overlapping genes were retained as markers of each cell subset
942 irrespective of treatment, and the geometric mean expression for each set of genes was calculated using
943 normalised bulk RNAseq data, thus generating subset scores for each bulk RNAseq sample. Pearson's
944 correlation was used to determine the accuracy of this scoring approach for each subset, showing good
945 concordance for all subsets. **(b)** As a further validation of the bulk RNAseq scores, subset scores across
946 n=399 samples were correlated against participant age using a mixed linear model, controlling for cycle
947 as a fixed variable; lmer(Score ~ Age+(1|Cycle)). **(c)** Changes in mitotic scores at C1 (d0), C2 (d21) or
948 C4 (d63) of treatment (n=49 individuals, two-sided Wilcoxon-signed rank test). **(d)** Heatmap of
949 Spearman's rho values for correlations between bulk subset scores; filled boxes represent adjusted p-
950 value <0.05 upon Bonferroni's correction. **(e)** Change in clonal size with major phenotype in the given
951 subset at C1 and C2 (unpaired Wilcoxon test). For each clone, the subset in which most of its members
952 were present was designated as the predominant phenotype for that clone; clones equally distributed
953 across multiple subsets were excluded. Clones above the dotted line represent large clones occupying
954 size greater than 0.5% of the repertoire.

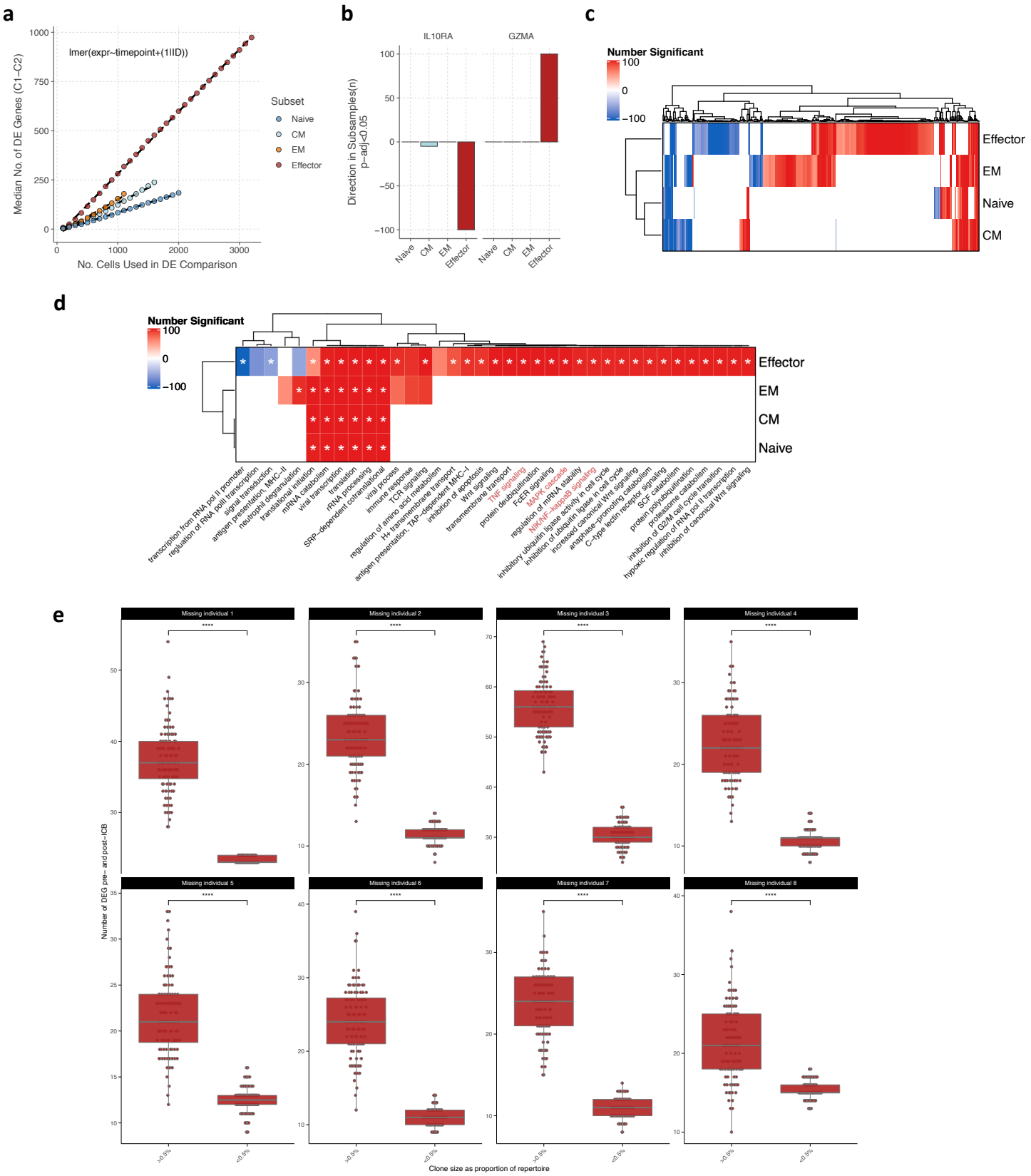

Supplementary Figure 3. Differential expression analysis across subsets and clone sizes. (a) Median number of differentially expressed (DE) genes across 21 days of ICB in conventional T cell subsets, as per Fig 3a but using the annotated mixed linear model instead of the *FindMarkers* Seurat function to identify significantly modulated genes (Bonferroni's adjusted p-value <0.05). At each n-

value for number of cells, there was a significant difference across the subsets in the number of DE genes ($p<0.0001$, unpaired Wilcoxon test). **(b)** Differential modulation of *IL10RA* and *GZMA* across each subset using *FindMarkers* bootstraps. The number of times each of the specified genes was detected as significantly up- or downregulated across 100 bootstraps was plotted per subset (subsample of n=1100 cells, direction represents increased or decreased expression following ICB). **(c)** Heatmap of DE genes across each subset, detected in greater than 50/100 *FindMarkers* bootstraps. Intensity of shading indicates how many bootstraps the gene was detected in, and colour represents whether the gene was significantly up- or downregulated. **(d)** Heatmap of induced or suppressed GOBP pathways modulated in each subset, in more than 50/100 *FindMarkers* bootstraps; selected pathways highlighted in red. Pathways marked with an asterisk* represent those also found using an equivalent approach based on DE genes detected by the mixed linear model. **(e)** Number of differentially expressed genes pre- and post- treatment for large vs small ECs (red) sequentially omitting one individual each time. The EC cluster was subsampled to a constant size and the analysis bootstrapped 100x (unpaired Wilcoxon test).

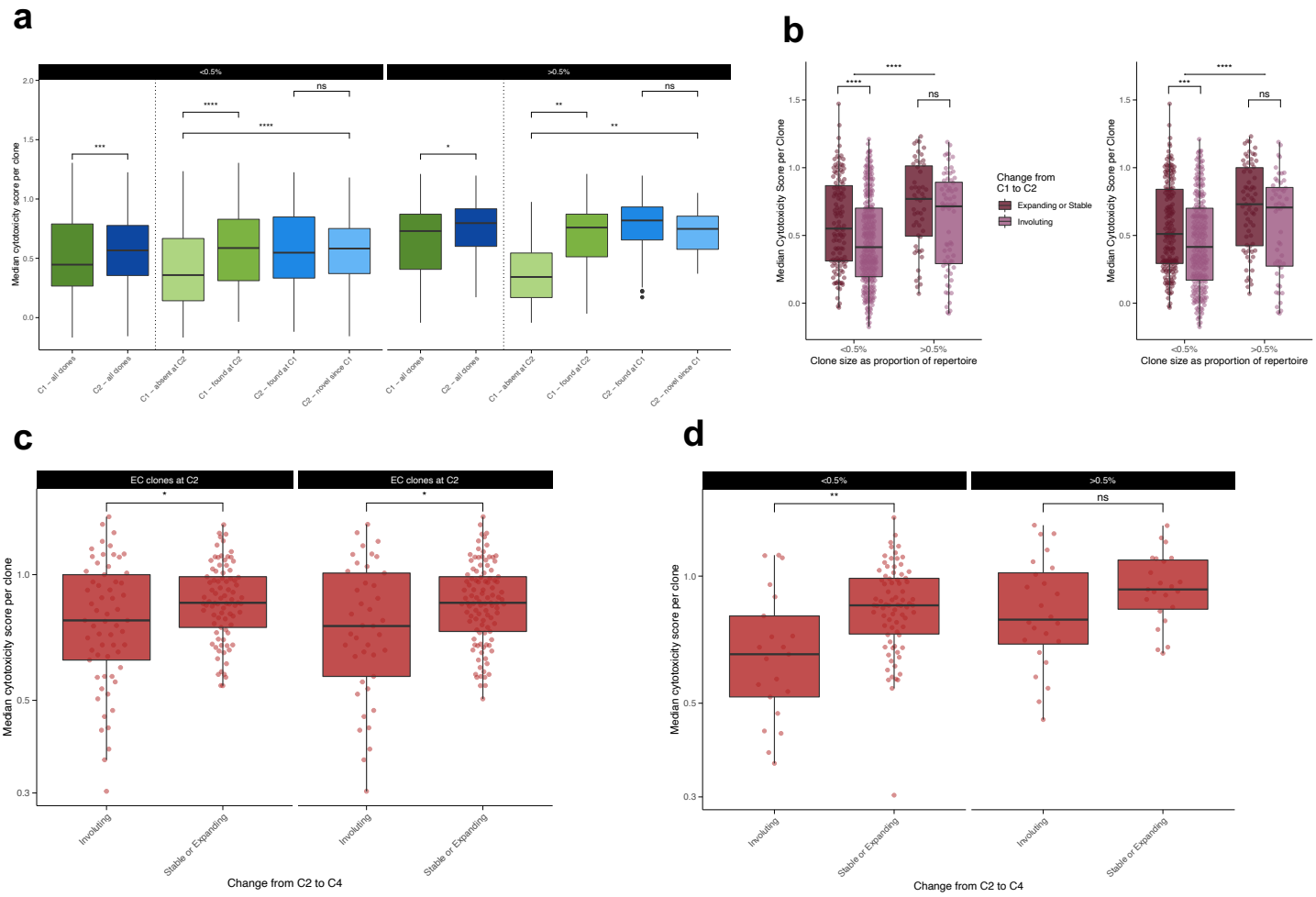

Supplementary Figure 4. Cytotoxic clones demonstrate propensity to persist post-ICB treatment. **(a)** Median cytotoxicity per clone for those found at both C1/C2 versus just at one timepoint, relative to all clones at C1 and C2. Clones were separated based on clonal size using a cut-off of 0.5% of the repertoire to denote large from small. **(b)** Median cytotoxicity per clone for those present at C1 that subsequently expand/remain stable (dark purple) or involute (light purple) by C2. Clones are separated based on size using a cut-off of 0.5% of the repertoire to denote large from small. Here, involuting clones are defined as those which are either 40% (left panel) or 60% (right panel) smaller at C2 compared to C1, whilst expanding/stable clones are those which, at C2, are within 40% or 60% of their baseline size. **(c)** Median cytotoxicity score per clone across EC clones found at C2 that subsequently expand/remain stable or involute by C4+. Here, involuting clones are defined as those which are either 40% (left panel) or 60% (right panel) smaller at C4+ compared to C2, whilst expanding/stable clones are those which, at C4+, are within 40% or 60% of their C2 size. **(d)** Median cytotoxicity per clone for EC clones found at C2 that subsequently expand/remain stable or involute by C4+, separated based on clonal size using a cut-off of 0.5% of the repertoire to denote large from small. For all data, Wilcoxon rank-sum tests used for all comparisons unless otherwise stated.

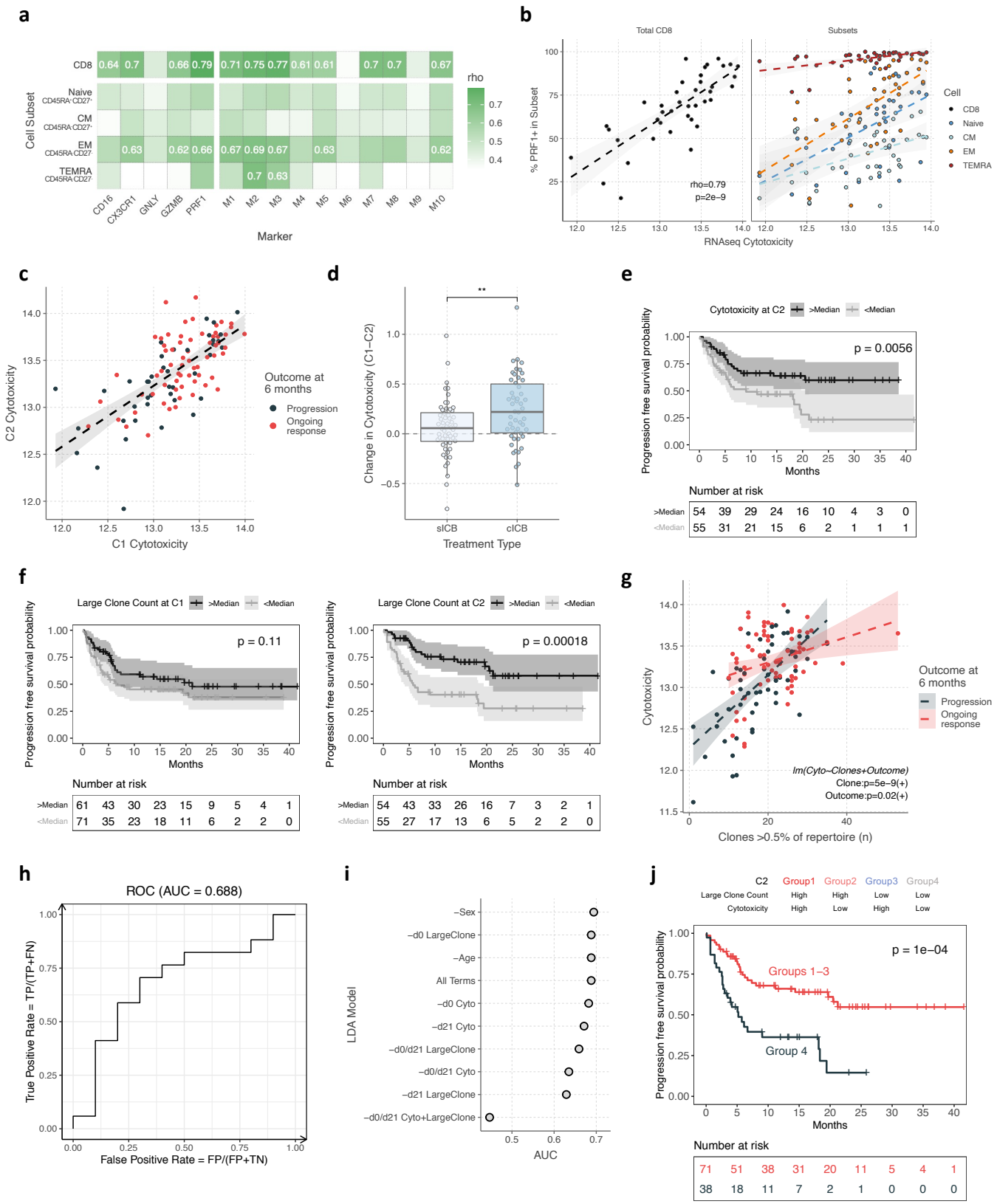

Supplementary Figure 5. CD8$^+$ cytotoxicity associations with flow cytometry, TCR analysis and clinical outcomes. (a) Heatmap of Spearman's correlations between bulk RNA-seq cytotoxicity and cytotoxic protein expression by flow cytometry across all CD8$^+$ T cells, or within CD8$^+$ cell subsets

(n=20 C1 and 20 C2 samples; gating indicated on axis). M1-M10 refers to combinatorial gates of cytotoxic proteins; all gating listed in Supplementary Table 9. The top 10 Spearman's rho values are displayed in the heatmap. **(b)** Spearman's correlation between bulk RNA-seq cytotoxicity and % $PRF1^+$ cells across all $CD8^+$ T cells (left) or within subsets (right). **(c)** Correlation between cytotoxicity at C1 and C2 (n=106 patients, Spearman's rank test). **(d)** Change in cytotoxicity in bulk cohort between C1-C2 based on ICB treatment type (n=106 patients, two-sided unpaired Wilcoxon-test). **(e-f)** Kaplan-Meier curve of progression-free survival in patients with d21 cytotoxicity **(e)**, or d0 (left) and d21 (right) large clone count **(f)** above median above median (n=132 patients or 109 patients at d0 or d21 respectively, two-sided log-rank test). **(g)** Linear effect model testing for correlation between C1 cytotoxicity, and large clone count and six-month clinical outcome, controlling for both as covariates (n=132 patients, positivity or negativity of estimate value indicated in brackets). **(h)** Receiver operating characteristic plot for a linear discriminant analysis (LDA) model for six-month clinical outcome, incorporating d0 and d21 large clone count and cytotoxicity, age and sex (n=106 patients). Individuals were randomly separated into independent training (n=78) and test (n=28) sets for cross-validation. **(i)** Area under curve (AUC) values for the LDA model in (h) upon omitting various predictor variables. **(j)** Progression free survival in patients separated by a combination of d21 large clone count and cytotoxicity (above/below median) (n=109, two-sided log-rank test).

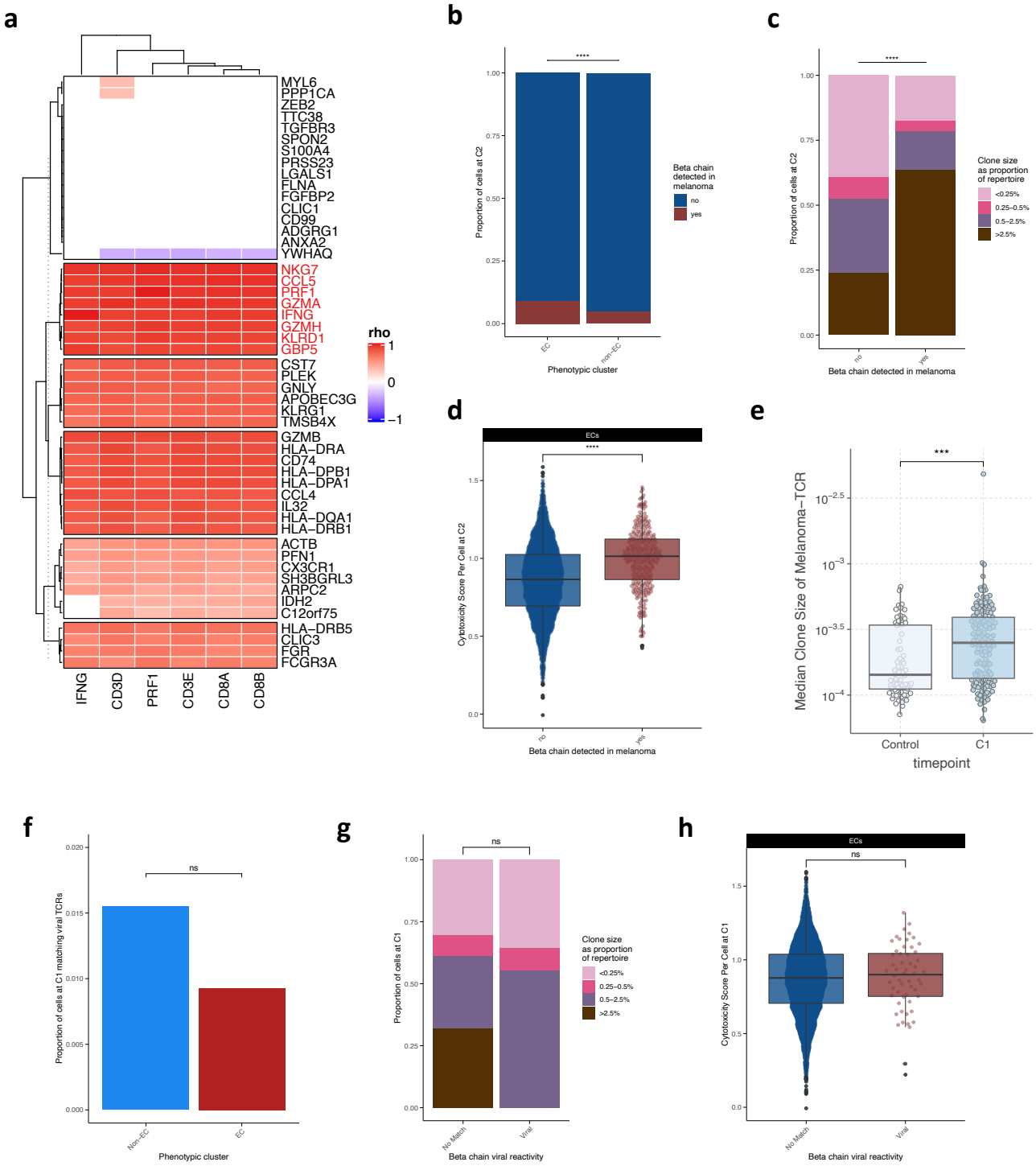

Supplementary Figure 6. Intratumoral analysis of T cell clonality and cytotoxicity. (a) Heatmap of Spearman's correlations based on tumour RNAseq data from Riaz et al. 2017 between *CD3D, CD3E, CD8A, CD8B, IFNG* and *PRF1* gene expression and 50 genes used in the calculation of peripheral cytotoxicity score, with the selected module of most-correlated genes used in the calculation of intratumoral T cell cytotoxicity highlighted in red. **(b)** Proportion of ECs compared to non-ECs at C2 that carry a tumour-infiltrating TCRB chain, as identified by TCRseq of resected melanomas by Pruessman et al. 2020*(26)* (Fisher's exact test). **(c)** ECs at C2 that are either tumour-infiltrating or not, separated by clonal size; Fisher's exact test for the proportion of large clones (>0.5%) compared to small clones found in the tumour-infiltrating and not-tumour-infiltrating compartments. **(d)**

1025 Cytotoxicity scores of ECs at C2 categorised by whether they carry a tumour-infiltrating TCRB chain
1026 or not (unpaired Wilcoxon test). **(e)** TCRB chains were matched with the TCR sequences in the bulk
1027 cohort and the median clone size of matching clones per individual was compared between healthy
1028 controls and melanoma patients (unpaired Wilcoxon test). **(f-h)** TCR chains from the single-cell VDJ
1029 data were matched with viral TCR sequences from VDJdb and the relative subset enrichment **(f**; Fisher's
1030 exact test**)**, clonal size groupings in ECs **(g**; Fisher's exact test for proportion of clones >0.5% across
1031 groups) and cellular cytotoxicity in ECs **(h**; unpaired Wilcoxon test**)** was similarly compared between
1032 viral-matching and non-matching cells.
1033

1034